

1

2 PNAS

3

4 Main Manuscript for

5 Elucidation of a dynamic interplay between a beta-2 adrenergic receptor,
6 its agonist and stimulatory G protein

7

8 Yanxiao Han¹, John R.D. Dawson^{1,2}, Kevin R. DeMarco¹, Kyle C. Rouen^{1,2}, Slava Bekker^{3,1},

9 Vladimir Yarov-Yarovoy^{1,5}, Colleen E. Clancy^{1,4}, Yang K. Xiang^{4,6}, Igor Vorobyov^{1,4*}

10 ¹Department of Physiology and Membrane Biology, ²Biophysics Graduate Group, ⁴Department of
11 Pharmacology, and ⁵Department of Anesthesiology and Pain Medicine,
12 University of California, Davis, Davis, CA, 95616

13 ³Department of Science and Engineering, American River College, Sacramento, CA, 95841

14 ⁶VA Northern California Health Care System, Mather, CA 95655

15 * Corresponding author Email: ivorobyov@ucdavis.edu

16 **Author Contributions:** Y.H., J.R.D.D., K.R.D., S.B., V.Y.-Y., C.E.C., Y.K.X., and I.V. designed
17 research; Y.H., J.R.D., K.R.D., S.B. and I.V. performed research; Y.H., K.C.R. and I.V. analyzed
18 data; and Y.H., K.C.R., V.Y.-Y., C.E.C., Y.K.X., and I.V. wrote the paper.

19 **Competing Interest Statement:** the authors declare no conflict of interest

20 **Classification:** Biophysics and Computational Biology

21 **Keywords:** G protein-coupled receptor; G protein; norepinephrine; sympathetic nervous system;
22 molecular dynamics

23

24 **This PDF file includes:**

25 Main Text
26 Figures 1 to 5
27 Tables 1 to 2
28

29 **Abstract**

30 G protein-coupled receptors (GPCRs) represent the largest group of membrane receptors for
31 transmembrane signal transduction. Ligand-induced activation of GPCRs triggers G protein
32 activation followed by various signaling cascades. Understanding structural and energetic
33 determinants of ligand binding to GPCRs and GPCRs to G proteins is crucial to the design of
34 pharmacological treatments targeting specific conformations of these proteins to precisely control
35 their signaling properties. In this study we focused on interactions of a prototypical GPCR, beta-2
36 adrenergic receptor (β_2 AR), with its endogenous agonist, norepinephrine (NE), and the
37 stimulatory G protein (G_s). Using molecular dynamics (MD) simulations, we demonstrated
38 stabilization of cationic NE, NE(+), binding to β_2 AR by G_s protein recruitment, in line with
39 experimental observations. We also captured the partial dissociation of the ligand from β_2 AR and
40 the conformational interconversions of G_s between closed and open conformations in the NE(+)-
41 β_2 AR- G_s ternary complex while it is still bound to the receptor. The variation of NE(+) binding
42 poses was found to alter G_s α subunit ($G_s\alpha$) conformational transitions. Our simulations showed
43 that the interdomain movement and the stacking of $G_s\alpha$ $\alpha 1$ and $\alpha 5$ helices are significant for
44 increasing the distance between the $G_s\alpha$ and β_2 AR, which may indicate a partial dissociation
45 of $G_s\alpha$. The distance increase commences when $G_s\alpha$ is predominantly in an open state and can
46 be triggered by the intracellular loop 3 (ICL3) of β_2 AR interacting with $G_s\alpha$, causing
47 conformational changes of the $\alpha 5$ helix. Our results help explain molecular mechanisms of ligand
48 and GPCR mediated modulation of G protein activation.

49 **Significance Statement**

50 G protein-coupled receptors (GPCRs) and G proteins work together to transmit signals from
51 various hormone and neurotransmitter molecules across cell membranes, and their activation and
52 subsequent dissociation initiate a cascade of downstream signaling events resulting in
53 modulation of cellular behavior. Here we studied interactions of a prototypical GPCR, beta-2
54 adrenergic receptor in its active state, with neurotransmitter norepinephrine and stimulatory G
55 protein using multi-microsecond-long atomistic computer simulations to understand how energetic
56 and structural changes in this system could initiate cellular signaling. Our results provided us with
57 intrinsic molecular mechanisms, which may control G protein dissociation from GPCRs, and
58 highlighted the importance of protein domain and ligand dynamics in this crucial biological
59 process.

60

61

62 **Main Text**

63

64 **Introduction**

65

66 GPCRs transduce intracellular signaling via coupling to G proteins. In the heart, sympathetic
67 nervous system (SNS) activation increases cardiac output to supply the body with oxygenated
68 blood by raising the heart rate, the force of contraction, and conduction rate (1). SNS activation in
69 the cardiovascular system is triggered by binding of two catecholamine neurotransmitters,
70 norepinephrine (NE) and epinephrine (Epi), to specific cell surface adrenergic receptors (β ARs in
71 human heart), which belong to the superfamily of GPCRs (2). There are three β AR subtypes in
72 the nonfailing human heart (75% – 80% of β_1 , 15% – 18% of β_2 , and 2% – 3% of β_3), regulating
73 cardiac rate and contractility by responding to NE and Epi (2, 3). Recently, β_2 AR has been the
74 focus of therapeutic interest, partly because of its relative preservation of expression in the failing
75 human heart (4). After binding to agonists, β_2 AR can activate the stimulatory G protein (G_s). G_s is
76 a heterotrimer consisting of an α subunit ($G_s\alpha$) and a tightly associated $\beta\gamma$ complex (5). The $G_s\alpha$
77 subunit harbors the guanine nucleotide-binding site and associates with the $\beta\gamma$ complex in the
78 inactive GDP-bound state (5). Binding of G_s to the agonist-bound β_2 AR results in activation and
79 dissociation of trimeric G proteins (5, 6). Both $G_s\alpha$ and $\beta\gamma$ can transduce a cascade of
80 downstream signaling events which eventually regulate cardiac rate and contractility (2, 4).
81 However, the molecular determinants and the dynamics of the ternary complex during receptor
82 signaling transduction remain incompletely understood.

83 The GDP release by G protein is a preparatory step of G protein activation which takes place
84 between two stable end-point states: one is referred as “closed-out” with G protein closed and its
85 β AR-interacting $\alpha 5$ helix outside the receptor, and the other is referred as “open-in” with G protein
86 fully open and the $\alpha 5$ helix coupled to the receptor. In 2011, Rasmussen et al. crystallized the first
87 high-resolution structure of β_2 AR bound G_s (β_2 AR- G_s) which is a ternary complex in the “open-in”
88 state consisting of a high affinity agonist (BI-167107), an active-state receptor, and G_s (7). There
89 $G_s\alpha$ subunit adopts an open state with a largely displaced α -helical domain ($G_s\alpha$ AH) and Ras-
90 like GTPase domain ($G_s\alpha$ Ras) (7). More recently, a cryo-EM structure of the β_1 AR- G_s complex
91 bound to another high-affinity agonist (isoproterenol) was solved, in which $G_s\alpha$ subunit adopts a
92 somewhat different but also open conformation (8). The agonist-bound structure is very distinct
93 from the crystal structure of the receptor-free closed $G_s\alpha$ -GTPy complex (7, 9). In another work,
94 an intermediate state of G_s between the GDP-bound G_s and GDP-free β_2 AR- G_s complex was
95 proposed by Liu et al. by crystalizing an active-state structure of the β_2 AR stabilized by the last 14
96 residues of the $G_s\alpha$ terminal $\alpha 5$ -helix (6). Su and Zhu et al. found that β_1 AR induces a tilting of
97 the $\alpha 5$ helix of $G_s\alpha$ which deforms the GDP/GTP-binding pocket and accelerates GDP release
98 (8). Goricanec et al. performed NMR spectroscopic characterization of an inhibitory $G\alpha$ subunit,
99 $G\alpha 1$, and showed that it adopts a more open conformation in the apo and GDP-bound forms, but
100 a more compact and rigid state in the GTP-bound form with no interaction to GPCR (5). They
101 proposed that the apo G_i protein eventually binds to GTP, leading to subunit dissociation and loss
102 of affinity to the receptor (5).

103 Meanwhile, there have also been multiple atomistic modeling and simulation studies of β AR
104 conformational dynamics and transitions (10-17), their interactions with G_s protein (18-24) and
105 other regulatory proteins (25-27) as well as endogenous ligand and drug binding (28-36) (recently
106 reviewed, e.g., in (37-39)). Dror et al. studied the structural basis for GDP/GTP exchange in G_s
107 protein coupled with or uncoupled from β_2 AR by combining long time scale MD simulation with
108 experimental validations (23). Alhadeff et al. explored the free-energy landscape of β_2 AR
109 activation using coarse-grained (CG) modeling using multiple receptor and G_s protein
110 conformational states (40). In a follow-up study, Bai et al. performed targeted MD simulations and
111 free energy analysis based on the β_2 AR- $G_s\alpha$ structure and found that the GDP could be released
112 during the half-opening of the binding cavity in the transition to the G_s open state; the potential
113 key residues on $\alpha 5$ were also validated by site-directed mutagenesis (41). Enhanced sampling

114 metadynamics simulations were used to predict energetics of small-molecule ligand binding to
115 β 2ARs and other GPCRs in good agreement with experimental affinities (42-45), but for the most
116 part did not focus on the G protein dissociation and conformational transitions.

117 In the current study, we explore the relationship between the dissociation of G_s from the β_2 AR and
118 $G_s\alpha$ conformational change and characterize the molecular determinants of how and when G_s
119 may dissociate from the receptor and how and why the G_s binding affects the endogenous
120 agonist, cationic norepinephrine, NE(+), affinity to the receptor. We performed multiple
121 microsecond-long all-atom MD simulations to study the molecular interactions within the ternary
122 NE(+) β_2 AR- G_s complex. We applied the open-in state based on PDB:3SN6 (7) as our simulation
123 starting point (Figure 1) and focused on capturing the molecular conformational changes
124 associated with dissociation of G_s from the receptor.

125 **Results and Discussion**

126 Two types of molecular systems were simulated: beta-2 adrenergic receptor (β_2 AR) and its
127 complex with the stimulatory G_s (β_2 AR- G_s). The cationic norepinephrine, NE(+), bound at the
128 orthosteric binding site, was present in each system. The snapshot of the β_2 AR- G_s system is
129 shown in Figure 1. Each system was embedded in a lipid bilayer hydrated by 0.15 M NaCl,
130 corresponding to physiological conditions in the extracellular medium and equilibrated for 90 ns
131 using restraints that were gradually reduced in the first 40 ns of these simulations. We then
132 performed much longer production runs. For β_2 AR, a 2.5 μ s Anton 2 (Anton) unrestrained MD
133 simulations and three Gaussian accelerated MD (GaMD) runs (600 ns each, 1800 ns in total)
134 were performed. For β_2 AR- G_s system, four different Anton runs (5.0 μ s each for run 1, run 2, and
135 run 4; 7.5 μ s for run 3) and three GaMD runs (600 ns each, 1800 ns in total) were performed (see
136 Table S1). As we observed NE(+) partial dissociation after 4.5 μ s in Anton run 3, we extended it
137 to 7.5 μ s. Based on the simulation trajectories, we first checked the dominant and secondary
138 NE(+) binding poses in the β_2 AR and analyzed the role of G_s coupling in stabilizing the NE(+)
139 binding. Then, we assessed the conformational changes in the α subunit of G_s ($G_s\alpha$) upon
140 coupling with β_2 AR. The intracellular loop 3 (ICL3) of β_2 AR was found to be essential in
141 interacting with $G_s\alpha$ and causing a conformational change in the α 5 helix of $G_s\alpha$. The induced α 5
142 helix conformational change controls the formation of an active-state receptor – G protein
143 complex. To find the molecular determinants of $G_s\alpha$ conformational changes, structural
144 parameters were analyzed, including opening/closing of $G_s\alpha$ and the distance between two $G_s\alpha$
145 domains. The geometric centers were used for all the distance and angle measurements. Finally,
146 we analyzed distribution of those parameters converting them to two-dimensional free energy
147 profiles to explore low-energy pathways for $G_s\alpha$ conformation changes and its dissociation from
148 β_2 AR. We also performed a posteriori implicit-solvent molecular mechanics Poisson-Boltzmann
149 surface area (MM-PBSA) calculations to estimate β_2 AR binding to NE and G_s .
150

151 1. *Binding affinity of NE(+) to β_2 AR and β_2 AR- G_s*

152 The starting point of our β_2 AR- G_s simulations is the open-in $G_s\alpha$ state with $G_s\alpha$ in a fully open
153 conformation and its α 5 helix intruded into the intracellular part of the active-state β_2 AR (see
154 Figure 1) which is based on the agonist-bound X-ray structure of the complex (PDB ID: 3SN6)
155 (7). In that study Rasmussen et al. discovered that, in the ternary complex, G_s binding increased
156 the agonist binding affinity about 100-fold compared with β_2 AR alone and that agonist binding
157 promotes interactions of β_2 AR with GDP-bound G_s heterotrimer, leading to the exchange of GDP
158 for GTP followed by the functional dissociation of G_s into $G_s\alpha$ -GTP and $\beta\gamma$ subunits (7).
159 Therefore, understanding the effect of G_s on the agonist binding is crucial. We performed multiple
160 microsecond-long unbiased MD simulations (Anton runs) for the NE(+) bound β_2 AR (referred to
161 as β_2 AR) and NE(+) bound β_2 AR in complex with G_s (referred to as β_2 AR- G_s) as shown in Table
162 S1. To verify some of the observations, we also performed three GaMD runs for each of the
163 above systems (Table S1).

164 We performed clustering for the NE(+) binding poses in the β_2 AR and β_2 AR- G_s based on their
165 microsecond-long Anton run trajectories. Five clusters were found in each case as shown in
166 Figure S1A – D. One representative pose with the lowest root-mean-square deviation (RMSD)
167 compared with other frames was selected for each cluster (Figure S1C – D) and shown in the
168 color matching histogram in Figure S1A – B. Figure 2 shows the NE(+) binding results based on
169 Anton runs. Figure 2A shows the initial and three special representative poses found in β_2 AR and
170 in β_2 AR- G_s systems. The time series of center-to-center distances between NE(+) and β_2 AR for
171 all runs are shown in Figure 2B with the three special representative poses matching the colors of
172 the plots. All other representative poses can be found in Figure S1C – D. Figure 2C (the gray
173 molecule) shows the initial pose, which is also the representative pose of the biggest cluster
174 (cluster 2 in Figure S1A) in the β_2 AR system. The amino acid residues in close contact with NE(+)
175 forming the binding pocket were identified based on the frames collected in this cluster. The close
176 contacts are defined as the amino acid residues within 3 Å of the NE(+) for more than half of the
177 total MD simulation frames. The number of NE(+) poses in cluster 2 accounts for the largest
178 proportion (28%) of the overall binding poses for β_2 AR, and it is the initial and dominant binding
179 pose in this system (referred as NE(+)d). The amino acid residues forming the binding pockets of
180 NE(+)d are D113^{3.32}, V114^{3.33}, and V117^{3.36} on transmembrane helix 3 (TM3), F193^{45.52} on ECL2,
181 S203^{5.42} and S207^{5.46} on TM5, F289^{6.51} and F290^{6.52} on TM6, N312^{7.39} and Y316^{7.43} on TM7,
182 among which D113^{3.32}, S203^{5.42} and N312^{7.39} form hydrogen bonds with NE(+). The residue
183 superscripts denote the Ballesteros-Weinstein (BW) numbering of GPCRs (46). The residues
184 forming the binding site of NE(+) on the active β_2 AR are mainly from helices TM3, TM5, TM6, and
185 TM7, which matches the findings of Dror et al. (12), where they observed that helices TM5, TM6,
186 and TM7 contribute to the shift of β_2 AR conformation between inactive and active states, while
187 the helix TM3, TM5, and TM6 interactions also play an important role in this process.

188 Figure 2D shows the representative binding pose of NE(+) (magenta molecule) in the second
189 biggest cluster (cluster 4) of β_2 AR (referred to as NE(+)s1). This binding pose is considered
190 special because it shows a different orientation from all other poses in β_2 AR and has the biggest
191 deviation from the initial binding pose of NE(+) in β_2 AR as shown in Figure S1C. It is also the 2nd
192 most abundant pose, existing in 24.7% of the simulation frames (Figure S1A). A similar NE(+)
193 binding pose (red in Figs. 2 and S1) is also identified in the β_2 AR- G_s system as cluster 5, which is
194 also the 2nd most abundant with 21.3% (see Figs. S1B and S1D). The residues in close contact
195 with NE(+)s1 are identified in the same way as stated previously. Compared with the binding
196 pocket of NE(+)d, four new ligand-binding residues appear in the case of NE(+)s1, which are
197 T110^{3.29} on TM3, Y174^{45.33} and R175^{45.34} on ECL2, and Y199^{5.38} on TM5. D113^{3.32}, V114^{3.33},
198 F193^{45.52}, N312^{7.39}, and Y316^{7.43} are preserved in the NE(+)s1 pocket, where D113^{3.32} and
199 N312^{7.39} form H-bonds with NE(+)s1, while V117^{3.36}, S203^{5.42}, S207^{5.46}, F289^{6.51} and F290^{6.52} are
200 not interacting with NE(+) in this pose.

201 Figure 2E shows a special representative binding pose of NE(+) (light-blue molecule), which is
202 captured in cluster 4 of β_2 AR- G_s system (Figure S1D) and is referred to as NE(+)s2 hereafter. It
203 shows an almost opposite orientation compared to NE(+)s1 (Figure 2D) and has an 8.85%
204 population for the β_2 AR- G_s and is not represented in the β_2 AR alone (see Figure S1). This binding
205 pose mostly corresponds to a low-value plateau in the NE(+) to β_2 AR distance for β_2 AR- G_s run 1
206 from ~2.8–5 μs, as shown by a blue curve in Figure 2B. Compared with NE(+)d (Figure 2C),
207 three new interacting residues (W286^{6.48} on TM6, L311^{7.38} and G315^{7.42} on TM7) are found, while
208 six residues (V114^{3.33}, F193^{45.52}, S203^{5.42}, S207^{5.46}, F290^{6.52}, and Y316^{7.43}) are missing in the
209 binding pocket of NE(+)s2. As noted above, the red NE(+) molecule shown in Figures 2A and 2B
210 is another binding pose of NE(+) similar to NE(+)s1 of β_2 AR but was found in β_2 AR- G_s cluster 5.
211 It corresponds to NE(+) position plateaus in β_2 AR- G_s run 3 at ~3.5 μs and 4.5 – 7.5 μs (red curve
212 in Figure 2B) as well as at 2.6 – 3.9 μs of run 4 (purple curve in Figure 2B).

213 The above results indicate that NE(+) can have different degrees of dissociation from its
214 dominant binding pose and pocket regardless of the G_s binding. However, those special binding

215 poses appear later during simulations in the β_2 AR- G_s cases compared to simulations with β_2 AR
216 alone, as shown in Figure 2B. The partial dissociation of NE(+) can be attributed to the β_2 AR
217 residue movements, evidenced by the significant variations of its RMSD values, as shown in
218 Figure S2B. We found three special representative binding poses out of ten clusters, and only
219 one special pose (shown in light-blue in Figure 2) moves deeper inside the β_2 AR (based on the
220 center-to-center distance) closer to the intracellular side. In two other special poses (shown as
221 red and magenta in Figure 2) we observed outward movement of NE(+) towards the extracellular
222 side, which may indicate its partial dissociation from the receptor. Most other poses, which are
223 dominant in both β_2 AR and β_2 AR- G_s simulations (Anton runs), are slight variations of the original
224 pose with different degrees of shifting or rotation. Similar results were found in the GaMD runs as
225 shown in Figure S3, where the representative binding poses were captured for both β_2 AR and
226 β_2 AR- G_s , except that the NE(+) in one of the β_2 AR GaMD runs almost completely dissociates
227 from β_2 AR as shown in Figures S4A and S4B (the gray molecule), and the full ligand dissociation
228 may be possible to sample in longer runs and/or using e.g., ligand GaMD (LiGaMD) approach
229 (47) to be explored in the follow-up studies.

230 In short, in all our MD simulations we observed partial NE(+) dissociation, which adopted
231 alternative binding positions in the receptor interior, in most cases closer to an extracellular side.
232 G_s association in β_2 AR- G_s complexes seems to stabilize NE(+) binding to the orthosteric site in
233 the β_2 AR, as was evidenced by its delayed partial dissociation (Figure 2B), although a random
234 fluctuation could potentially cause this delay. Ligand (antagonist) dissociation was also observed
235 in an adenosine A_{2A} receptor where a multistep ligand dissociation pathway featured by different
236 ligand poses during dissociation was suggested based on temperature-accelerated MD
237 simulation (48). Similarly, using GaMD, different binding poses were also revealed for a partial
238 agonist in the orthosteric pocket of a muscarinic receptor in the absence or presence of G protein
239 mimic (nanobody) (49). These studies suggest that multiple ligand binding poses may be
240 common in GPCR systems with or without bound G protein.

241 We also computed MM-PBSA binding energies between β_2 AR and NE(+) and RMSDs for β_2 AR
242 based on Anton runs, as shown in Table 1. In most runs of β_2 AR- G_s , free energies of binding
243 between β_2 AR and NE(+) are more favorable than that for β_2 AR, in agreement with the
244 experiment (7). The reason for the stabilized NE(+) binding in the β_2 AR- G_s complex can be
245 attributed to the stabilization of β_2 AR active state by the open G_s , suggested experimentally (7)
246 and by previous coarse-grained simulations (40). We checked the RMSDs for the β_2 AR (not
247 including the intracellular loops) alone and in the presence of G_s . Using the averaged β_2 AR
248 structure as the reference, we computed the mean RMSD value and its standard deviation (SD)
249 for each run (Table 1) using VMD (50). RMSD time series for the receptor, G_s protein, NE(+) and
250 the entire β_2 AR- G_s complex can be found in Figure S2. Half of the β_2 AR- G_s runs show lower
251 mean RMSD values compared with the β_2 AR alone. Moreover, all the SDs (a measure of the
252 amount of variation from the mean) for the β_2 AR- G_s cases are lower than that of β_2 AR alone,
253 indicating more stable conformations of β_2 AR in complex with G_s . These analyses confirm that
254 NE(+) binding to β_2 AR- G_s is more favorable than to β_2 AR alone due to the stabilized β_2 AR
255 structure in the complex with G_s . In a recent GaMD study it was also found that removal of the G
256 protein mimic leads to a conformational transition of a muscarinic receptor M_2 to an inactive state
257 along with multiple orthosteric ligand dissociation and binding events consistent with extensive
258 experimental and computational studies of other GPCRs (49).

259 The MM-PBSA binding energies between β_2 AR/ β_2 AR- G_s and NE(+) based on GaMD runs can be
260 found in Table S2. Due to the nature of GaMD simulations, where different boost potentials were
261 added to the β_2 AR and β_2 AR- G_s systems to accelerate dynamics of both the protein and NE(+), it
262 is impossible to compare the binding energies between β_2 AR and β_2 AR- G_s systems directly,
263 unless the energy values are reweighted properly. Despite this, it is still true that the most
264 displaced NE(+) binds weaker to the β_2 AR or β_2 AR- G_s , as demonstrated using non-reweighted
265 MM-PBSA ΔG values for β_2 AR-GaMD run 1 as well as β_2 AR- G_s -GaMD runs 2 and 3 (Table S2

266 and Figure S4). Since the reweighting of entropy turned out to be exceedingly noisy, we only
267 reweighted the MM-PBSA enthalpy, ΔH , term by using the distribution of interaction energies
268 based on a cumulant expansion (details can be found in the Materials and Methods section) as
269 shown in the last column of Table S2. The reweighed ΔH show somewhat different trends from
270 the non-reweighted ones, but still reflect the weaker NE(+) binding affinity in β_2 AR-GaMD run 1
271 and β_2 AR-G_s-GaMD runs 2 and 3.

272 **2. *G_s conformational changes after binding with β_2 AR***

273 After checking the effect of G_s on NE(+) binding to β_2 AR, we analyzed the conformational
274 changes of G_s when it couples with β_2 AR. In the published β_2 AR-G_s complex structure (PDB:
275 3SN6), used as a starting point of our simulations, the G_s α preserves an open state with the α -
276 helical domain (G_s α AH) largely displaced from the Ras-like GTPase domain (G_s α Ras) as shown
277 in Figure 1. The G_s α AH rotated as a rigid body with an angle of approximately 127° from the
278 domain junction compared to the crystal structure of the closed G_s α -GTP γ (PDB: 1AZT) (7, 9).
279 However, a different G_s α conformation was discovered in the complex of isoproterenol-bound
280 β_1 AR-G_s, which is partly based on cryo-EM, due to the dynamic nature of G_s α AH (8). The G_s α in
281 β_1 AR-G_s is less open compared with that in the crystalized β_2 AR-G_s complex (7) but still can be
282 considered as a fully open state in comparison with G_s α alone (PDB: 1AZT) (9). G_s α
283 conformational transitions were thoroughly tested via long-scale MD simulations by Dror et al.,
284 who found that the separation of G_s α Ras and G_s α AH domains occurs only in the absence of
285 β_2 AR, whereas GDP release can only be observed after restraining G_s α α 5 in the distal
286 conformation like that in the β_2 AR-G_s complex, indicating the need of an internal structural
287 rearrangement of the G_s α Ras to weaken its nucleotide binding affinity (23).

288 As shown in Figure 3 (based on Anton runs), we used the geometric center-to-center distance
289 (referred to as “distance” hereafter for all the distances) between the G_s α AH residue A161^{H.HD.5}
290 and G_s α Ras residue E299^{G.HG.6} as an indicator for the opening and closing of G_s α (the same one
291 as used in the work of Dror et al. (23)), e.g., a larger distance between A161^{H.HD.5} and E299^{G.HG.6}
292 indicates a more open G_s α conformation. The residues are labeled by residue number and
293 common G α numbering (CGN) system (51) in their superscripts. The systems corresponding to
294 different Anton simulations are referred to as runs (with GaMD runs labeled differently). If the
295 distance is greater than or equal to 55 Å, we define G_s α conformation as fully open; if the
296 distance is in the range of 45 Å – 55 Å, we define it as semi-open; if the distance is in the range of
297 35 Å – 45 Å then it is a semi-closed structure, and if the distance is less than or equal to 35 Å
298 then it is a closed structure.

299 Transition of G_s α from open to closed conformation was observed e.g., in a 5.0 μ s long MD run 1
300 of β_2 AR-G_s complex: the distance between A161^{H.HD.5} and E299^{G.HG.6} changes from 62 to 34 Å
301 (Figure 3A). Interestingly, such transition was not captured by the previous multi-microsecond
302 long MD simulations by Dror et al., instead, an opposite conformational change of GDP bound
303 G_s α , from closed to fully open conformation was observed but only in the receptor-free systems
304 (23). They proposed that this conformational transition favors the closed state in the absence of
305 the receptor (23). When it comes to the receptor bound case, they only sampled fully open and
306 nucleotide free G_s α during their multi-microsecond long MD simulations. They also proposed that
307 the loss of GDP after G_s binding to β_2 AR shifts the equilibrium toward a widely open G_s α state
308 (23).

309 In run 3, we observed a very dynamic conformational transition of G_s α between open and semi-
310 closed states in terms of A161-E299 distance as shown in Figure S7A. This conformational
311 transition to a semi-closed state also correlates with the increase in NE(+) to β_2 AR distance in
312 Figure 2B. Specifically, the decrease in G_s α A161-E299 distance during ~4.0-5.5 μ s in Figure
313 S7A seems to correlate with an increase in NE(+) to β_2 AR distance in Figure 2B, i.e. partial
314 agonist dissociation, especially evident after ~4.5 μ s. A similar, but less evident correlation can be
315 seen for β_2 AR-G_s run 4, where transient rearrangements of G_s α to a semi-closed state may be

316 related to NE(+) partial dissociation from ~2.6 to 3.9 μ s (cf. Figs. S7A and 2B). Interestingly, $G_s\alpha$
317 transition to a fully closed state in β_2 AR- G_s run 1 discussed above may eventually lead to a
318 decreased NE(+) to β_2 AR distance at ~2.8 μ s, i.e., agonist movement deeper towards the
319 intracellular side (Figure 2B). These trends indicate the potential correlation between NE(+)
320 binding poses and G_s conformational changes.

321 In another β_2 AR- G_s simulation run (run 2), we observed similar open $G_s\alpha$ conformation as was
322 observed in Dror et al.'s work (23) throughout the entire 5 μ s-long MD simulation (Figures 3B and
323 S7A). Interestingly, in that run we observed partial unwinding of the $G_s\alpha$ α 5 helix (referred to as
324 α 5), a key interaction site with the receptor (see Figure 3B and bottom inset). We correlate this
325 α 5 conformational transition with the interaction between $G_s\alpha$ and flexible ICL3 of the β_2 AR as will
326 be discussed below. Snapshots for other β_2 AR- G_s runs can be found in Figures S5 and S6,
327 where different levels of $G_s\alpha$ closing and opening, different $G_s\alpha$ conformations and interaction
328 details between α 5 and ICL3 are shown.

329 Due to its unstructured nature, ICL3 region is either unresolved or completely removed and
330 replaced by T4-lysozyme (T4L) in experimental structures (15). Thus, very limited experimental
331 (52) and simulation (15) studies have discussed the possible effect of ICL3 on the intrinsic
332 dynamics of the receptor. Ozcan et al. found through MD simulation that ICL3 contributes to a
333 transition of β_2 AR to a "very inactive" conformation (15). DeGraff et al. explored the function of
334 ICL3 of α_2 -adrenergic receptors in determining subtype specificity of arrestin interaction (52). Yet,
335 it is well accepted that direct interaction of ICL3 with G-proteins probably has a significant role in
336 the receptor's dynamics and the activation/inactivation pathways (12, 15). However, due to the
337 absence of ICL3 in receptor structures, its function is not well understood. We examined specific
338 interactions between ICL3 and $G_s\alpha$ α 5 as shown in the insets of Figure 3 and Figure S5 with the
339 key amino acid residues in close contact between ICL3 and α 5 labeled. K232, D234 and K235
340 are the common amino acid residues from ICL3 involved in the interactions with α 5 in both run 1
341 and run 2. Table S3 shows the number of amino acid residues in close contact between different
342 parts of the proteins. The amino acid residues in ICL3 run 2 interact more extensively with α 5
343 with 72.5% average percentage interaction time compared to those in run 1 with 65.7% average
344 percentage interaction time. With the partial unwinding of α 5 in run 2, the number of amino acid
345 residues in the entire β_2 AR in close contact with α 5 is reduced to 22 with 85.0% average
346 percentage interaction time compared to 26 amino acid residues with 86.7% average percentage
347 interaction time in run 1, indicating partial dissociation of α 5 from the β_2 AR interior in run 2. These
348 analyses suggest that ICL3 involvement may trigger the conformational change of $G_s\alpha$ α 5, which
349 favors the dissociation of α 5 from the β_2 AR interior. Moreover, the conformational change of α 5 is
350 not correlated with the opening and closing of $G_s\alpha$, because we observed no significant changes
351 in α 5 conformation with closed $G_s\alpha$ in run 1 (Figure 3A), with partially open $G_s\alpha$ in runs 3 and 4
352 shown in Figure S5, and with open $G_s\alpha$ in the GaMD simulations (Figure S6). An important
353 question arises here: is there any correlation between different protein domains and what is the
354 relationship between the G_s conformational changes and its dissociation?

355 To answer this question, we performed analysis of time series for multiple distances and angles
356 between different protein residues and domains based on Anton runs as shown in Figure S7. The
357 average values of those distances and angles based on the last 2 μ s simulation for each run are
358 shown as scatter plots in Figures 4A and 4B. Figure S7A shows the time series of A161 – E299
359 distance. A special attention should be given to run 3, where the distance between A161 – E299
360 (51 \AA at the end of the run) indicates a partially open structure, but it represents a closed $G_s\alpha$ as
361 shown in Figure S5A, because the $G_s\alpha$ AH domain flipped upwards with A161 pointing up. We
362 then analyzed an angle between two vectors representing $G_s\alpha$ AH and $G_s\alpha$ Ras domains
363 indicating their relative orientation (Figure S7B). As shown in Figure 4C, vector 1 goes through
364 the centers of the $G_s\alpha$ AH domain and residue A161 and vector 2 goes through the centers of the

365 $G_s\alpha$ Ras domain and residue E299. Time series of $G_s\alpha$ AH – $G_s\alpha$ Ras center-to-center distance,
366 NPxxY – α 5 distance, β_2 AR – α 5 distance, and α 1 – α 5 distance are shown in Figures S7C-S7F.

367 As demonstrated using different distance and angle measurements in Figures 4 and S7, we
368 captured different conformations of $G_s\alpha$ in our multiple microsecond-long Anton simulations for
369 β_2 AR- G_s . The closing/opening conformational transition of $G_s\alpha$ is due to the movement of $G_s\alpha$ AH
370 relative to $G_s\alpha$ Ras. $G_s\alpha$ AH moves more like a rigid body as shown in RMSD plots when this
371 domain is aligned with β_2 AR or itself (Figure S8), which is in line with experimental findings (7,
372 53). The initial distance between A161 and E299 is about 62 Å based on the crystal structure
373 PDB: 3SN6. In run 1 (Figure S7A), we mostly captured the closed $G_s\alpha$, resembling the closed
374 inactive $G_s\alpha$ (PDB: 1AZT) (9), with the final distance of ~ 34 Å, as shown in Figure 3A. In run 2,
375 $G_s\alpha$ goes through a short period of partial closing with a minimum distance of ~ 47 Å at the very
376 beginning of the run, but the dominant conformation is fully open with a distance of ~ 64 Å (Figure
377 S7A and Figure 3B). In both run 3 and run 4, $G_s\alpha$ shows dynamical nature, switching between
378 fully open and semi-open states (Figure S7A). The $G_s\alpha$ AH flexibility is a reason for its low electron
379 density in the recent cryo-EM structure of the β_2 AR- G_s complex (8, 53). As mentioned in the
380 previous section, run 3 shows the flip up $G_s\alpha$ AH orientation, but it cannot be identified by A161 to
381 E299 distance. Thus, we analyzed the angle between $G_s\alpha$ AH and $G_s\alpha$ Ras domains and the
382 distance between the $G_s\alpha$ AH and $G_s\alpha$ Ras centers (Figures S7B and S7C). The angle is defined
383 by two vectors shown in Figure 4C. This angle weakly correlates with the opening and closing of
384 $G_s\alpha$ (Figure 4A), specifically, the big separation of A161 and E299 in run 2 does not guarantee a
385 large interdomain angle, indicating seemingly random drifting of the domains in 3D space during
386 conformational change of $G_s\alpha$. The Pearson correlation coefficients (Table S4), r , were calculated
387 among the data points in Figures 4A and 4B collected from the average values of the last 2 μ s of
388 each Anton runs. The value of r for the interdomain angle and A161 – E299 distance is 0.61
389 validating a relatively weak correlation.

390 To track a possible partial dissociation of G_s from β_2 AR, we analyzed the distance between $G_s\alpha$
391 helix α 5 and the conserved motif NPxxY in β_2 AR's transmembrane domain 7 (TM7) (Figure S7D)
392 as done by Miao et al. in their GaMD simulations for different GPCR systems, adenosine
393 receptors (54). Our β_2 AR- G_s Anton runs 1 and 2 show almost identical displacement of α 5 with
394 the largest dissociation distance among all the runs, but this does not match with our previous
395 analysis of dissociation in terms of the number of amino acid residue contacts (Table S3), where
396 run 2 shows a more dissociated β_2 AR- G_s complex than run 1. Thus, we think the NPxxY to α 5
397 distance may be not suitable to accurately predict displacement of α 5 from β_2 AR in our systems,
398 because NPxxY motif can be easily affected by the relative movement of TM7 to other TMs in our
399 systems, which adds random noise into the measured distances. As α 5 is a major element of the
400 G protein - GPCR interacting interface (8, 23, 41, 54), researchers in a recent study used it as a
401 cognate peptide to probe the kinetics of its binding to and activation of β_2 AR, which is at least on
402 the order of seconds (55), much longer than a time scale of our MD simulations. Despite this, we
403 think that the center-to-center distance between β_2 AR and α 5 may be suitable to check the
404 displacement of α 5 from β_2 AR which can be used as a sign for a commencement of G_s
405 dissociation, and the corresponding plot is shown in Figure S7E. However, there is still no
406 obvious correlation between the $G_s\alpha$ conformational change and β_2 AR- G_s partial dissociation as
407 the values of r between β_2 AR – α 5 distance and A161 – E299 distance is 0.53, $G_s\alpha$ interdomain
408 orientation angle is 0.07, $G_s\alpha$ AH – $G_s\alpha$ Ras distance is 0.46 (Table S4, row 4). These results
409 indicate that closing or opening of $G_s\alpha$ by itself cannot control the suggested partial dissociation
410 of G_s from β_2 AR. Instead, the internal arrangement of protein secondary structure elements may
411 matter. To validate our assumption, we further analyzed the center-to-center distance between
412 $G_s\alpha$ helices α 1 and α 5 as shown in Figure S7F (the illustration of these two helices in $G_s\alpha$ is
413 shown in Figure 4D). We found a strong negative correlation between α 1 – α 5 distance and β_2 AR
414 – α 5 distance with the r of -0.80. The temporal variation of value of r between α 1 – α 5 distance
415 and β_2 AR – α 5 distance in each Anton run was also calculated in terms of lag time (Figure S9A).
416 The negative correlation was found in runs 2, 3 and 4 when the lag time is less than 1 μ s and

417 where conformational transition is clearly seen in the latter two runs. Thus, we think the stacking
418 of $\alpha 1$ and $\alpha 5$ mostly causes the dislocation of $\alpha 5$ from β_2 AR. Importantly, we also found that the
419 opening of $G_s\alpha$ (indicated by $G_s\alpha$ AH – $G_s\alpha$ Ras interdomain distance and A161 to E299 distance)
420 is negatively correlated with the $\alpha 1$ – $\alpha 5$ distance with relatively large r values of –0.65 (Table S4,
421 row 5). This indicates that the opening of $G_s\alpha$ in the nucleotide free state is related to the stacking
422 of $\alpha 1$ and $\alpha 5$ following the dislocation of $\alpha 5$ from β_2 AR. However, the direct correlation between
423 $G_s\alpha$ AH – $G_s\alpha$ Ras interdomain distance and β_2 AR – $\alpha 5$ distance with an r of 0.46 is not as strong
424 as expected, indicating the importance of the internal domain rearrangement in the suggested
425 partial dissociation of G_s . The role of $\alpha 1$ and $\alpha 5$ movements has been highlighted in the structural
426 analysis of β_2 AR – G_s coupling/association and GDP release processes (56). Specifically, it was
427 found that $\alpha 5$ interacts with $\alpha 1$, $\beta 2$ and $\beta 3$ through highly conserved hydrophobic contacts in the
428 GDP-bound closed $G_s\alpha$, and structural perturbation of $\alpha 1$ accelerates GDP release and opening
429 of inactive $G_s\alpha$ (56). Here, in our study of G_s partial dissociation, $\alpha 1$ and $\alpha 5$ were found to be
430 important in regulating the conformational change of $G_s\alpha$. The stacking of $\alpha 1$ and $\alpha 5$ may cause
431 the opening of $G_s\alpha$ (or vice versa), pulling the $\alpha 5$ away from the interior part of β_2 AR, which
432 facilitates the G_s dissociation. In the GaMD runs, the $G_s\alpha$ is almost always in a fully open state
433 (Figures S6 and S10), except at the end of β_2 AR- G_s -GaMD-run2 where a semi-open state
434 appears. We did not see large $G_s\alpha$ conformational changes in the enhanced sampling GaMD
435 runs as observed in the unbiased Anton runs 1 and 4 which could be due to random fluctuations.
436 We do not anticipate any correlations for the interdomain distances when there is no obvious $G_s\alpha$
437 conformational change. In our study we used general GaMD methodology, which boosts the
438 overall potential of the system (57) and may not have been sufficient to trigger a $G_s\alpha$
439 conformational transition. Using a more directed approach such as protein–protein interaction-
440 GaMD (PPI-GaMD) (58) may solve this issue in the follow-up studies.

441 We then calculated the free energy or potential of mean force (PMF, in kcal/mol) 2D profiles (see
442 Figures 5 and S11-S12) based on $G_s\alpha$ conformation and its β_2 AR partial dissociation to further
443 validate the correlation analyzed in the previous section. As shown in Figure 5A, the 2D PMF for
444 the A161 – E299 distance on the x axis versus the β_2 AR – $\alpha 5$ distance on the y axis exhibits two
445 free energy minima, the closed $G_s\alpha$ (at $x = \sim 32$ Å) and the open $G_s\alpha$ (at $x = \sim 58$ Å). There is a
446 small free energy barrier of about 2 – 3 kcal/mol between the two minima, but the open state is
447 more energetically favorable, which is in line with the proposition in the earlier work of Dror et al.
448 (23). Interestingly, only one minimum was found in the GaMD run (Figure S11A) at an even more
449 open $G_s\alpha$ state ($x = \sim 67$ Å). It can also be seen that the open $G_s\alpha$ (Figure 5A) favors a larger
450 distance between $\alpha 5$ and β_2 AR compared with the closed $G_s\alpha$. Notably, there are also more
451 chances for the dislocation of $\alpha 5$ from its β_2 AR binding site when $G_s\alpha$ is open because of the
452 bigger area within the 0.5 kcal/mol low-energy contour line associated with the open state.
453 Similarly, Figure S12E shows the 2D PMF for the $G_s\alpha$ AH – $G_s\alpha$ Ras interdomain distance versus
454 the β_2 AR – $\alpha 5$ distance, also indicating a larger chance of $\alpha 5$ dislocation in the open state.
455 However, the open $G_s\alpha$ conformation by itself cannot guarantee the dissociation, as the
456 structures in runs 3 and 4 at around 3 μ s (Figure S7A) correspond to the open $G_s\alpha$, but they are
457 not in a suggested partially dissociated state (Figure S7E). We previously proposed that some
458 internal structural rearrangements may occur during the opening and closing of $G_s\alpha$, triggering
459 the dissociation. We again found that the relative movement between $G_s\alpha$ helices $\alpha 5$ and $\alpha 1$ is
460 well correlated with the dislocation of $\alpha 5$ from β_2 AR. As shown in Figure 5B, decreasing the
461 distance between $G_s\alpha$ $\alpha 5$ and $\alpha 1$, as marked with the yellow arrow, can lead to the dislocation of
462 $\alpha 5$ with minimal energy barriers (~ 0.1 kcal/mol). Also, Figure S12B shows the 2D PMF for the
463 $G_s\alpha$ AH – $G_s\alpha$ Ras interdomain distance versus $G_s\alpha$ $\alpha 1$ – $\alpha 5$ interhelical distance, which exhibits a
464 negative correlation in line with the Pearson correlation coefficient calculations in the previous
465 section. These analyses indicate that the stacking of $\alpha 1$ and $\alpha 5$ helices can be the molecular
466 determinant for the partial dissociation of G_s from β_2 AR in the absence of guanine nucleotide
467 binding. The interaction between $\alpha 1$ and $\alpha 5$ was previously found to be important in the allosteric

468 activation of $G_s\alpha$ using structural and phylogenetic analyses (51). The interruption of the contacts
469 between $\alpha 1$ and $\alpha 5$ was found to be the key step for GDP release during the association of $G_s\alpha$
470 to its receptor (51). And, in our study we observed that the interaction between $\alpha 1$ and $\alpha 5$ favors
471 suggested partial dissociation of $G_s\alpha$ from its receptor, thus sharing similar structural
472 rearrangements to their association process. This indicates that interaction between $\alpha 1$ and $\alpha 5$
473 could be a molecular control for the association and dissociation kinetics of $G_s\alpha$ and $\beta_2\text{AR}$.

474 To estimate the relative binding affinities between the G_s and $\beta_2\text{AR}$, we calculated corresponding
475 MM-PBSA interaction energies² as shown in Table 2. These results can be compared with
476 different conformations of $G_s\alpha$ (Figures 3 and S5) to give insights into the correlation between G_s
477 conformation and its possible partial dissociation from $\beta_2\text{AR}$. As discussed previously, during the
478 last 2 μs , run 1 corresponds to the fully closed $G_s\alpha$; run 2 has a fully open $G_s\alpha$; in run 3 and run 4,
479 $G_s\alpha$ is very dynamic, transitioning between open and intermediate states, which makes predicting
480 the trends in MM-PBSA interaction energy challenging. Run 1 with the final closed G_s
481 conformation shows the lowest (most favorable) free energies of binding, while run 2 with a fully
482 open structure shows relatively higher (less favorable) binding free energy, indicating more
483 chances of G_s dissociation with the open state. This result is in line with the 2D PMF analysis
484 (discussed above) where the minimum for $G_s\alpha$ open states span a larger range of distances
485 between $G_s\alpha$ $\alpha 5$ and $\beta_2\text{AR}$ indicating a larger chance for dissociation. Moreover, we found fewer
486 interacting amino acid residues between $\alpha 5$ and $\beta_2\text{AR}$ and a bent $\alpha 5$ conformation in run 2 with
487 an open state compared with run 1 where $G_s\alpha$ is mostly in a closed state. Also, the number of
488 interacting amino acid residues at the G_s – $\beta_2\text{AR}$ binding interface shows a clear trend of
489 decrease in the longer run, run 3, also possibly suggesting a partial G_s dissociation (Figure S13).
490 Altogether, we found that the opening of $G_s\alpha$ favors its partial dissociation from $\beta_2\text{AR}$ but is not
491 sufficient. The interdomain rearrangement, namely, the stacking of $G_s\alpha$ helices $\alpha 1$ and $\alpha 5$ is
492 necessary for the partial G_s dissociation process. We have to mention that we only considered
493 nucleotide-free and receptor-bound open-in G_s initial state in this work. The effect of GTP/GDP
494 binding to the G_s conformational transitions and dissociation will be evaluated in a follow-up
495 study.

496
497 **Conclusions**
498

499 Combining all-atom multi-microsecond-long MD simulations with a posteriori implicit-solvent MM-
500 PBSA calculations, we found that G_s binding to $\beta_2\text{AR}$ can stabilize the NE(+) binding to $\beta_2\text{AR}$
501 through stabilizing the structure of the active $\beta_2\text{AR}$ conformation. Different binding poses and
502 partial dissociation of NE(+) were captured in both free and G_s bound $\beta_2\text{AR}$ systems. The partial
503 dissociation of NE(+) can be attributed to the altered $\beta_2\text{AR}$ structure due to its interactions with
504 G_s , evidenced by the variances of $\beta_2\text{AR}$ RMSD values. The wagging of NE(+) binding to $\beta_2\text{AR}$,
505 i.e., presence of alternative binding poses closer to extra- or intracellular sides than the
506 orthosteric binding site, was found to be related to the $G_s\alpha$ conformational transition to a semi-
507 closed or closed state. Using all-atom MD simulations, we also observed interaction between
508 $\beta_2\text{AR}$'s ICL3 and G_s which caused the partial unwinding of the $G_s\alpha$ $\alpha 5$ helix in the open-in state of
509 this subunit, suggesting the important role of ICL3 in the G_s dissociation. ICL3 was included in our
510 models but usually missing in the available PDB structures (7, 8, 53), thus very limited information
511 can be found about its function in related works (6, 12, 41). We also captured multiple closed and
512 semi-closed conformations of the $G_s\alpha$ subunit in the $\beta_2\text{AR}$ - G_s system. These conformations are
513 absent in previous simulation works (6, 23, 40, 41) and hard to obtain from experiments due to
514 the highly dynamic nature of $G_s\alpha$ (8, 56). Our simulation data indicate the possibility of G_s
515 closing before its partial dissociation from $\beta_2\text{AR}$, which was not observed in previous simulation
516 studies to the best of our knowledge. However, the closed $G_s\alpha$ conformation is less favorable
517 compared with the open one in promoting the dislocation of $G_s\alpha$ $\alpha 5$ from its $\beta_2\text{AR}$ binding site.
518 Instead, the internal $G_s\alpha$ domain stacking between helices $\alpha 1$ and $\alpha 5$ was found to be

519 necessary. We found that the open $G_s\alpha$ favors a more stacked $\alpha 1$ and $\alpha 5$ arrangement, which
520 can drive the dissociation of $G_s\alpha \alpha 5$ from the receptor. Yet, the binding of guanine nucleotides
521 may have a different effect on the G protein conformational changes and dislocation of $G_s\alpha \alpha 5$
522 from its receptor binding site, which will be evaluated in our subsequent studies. The results of
523 this study may help explain molecular determinants and underlying mechanisms on why bound
524 G_s protein can stabilize NE(+) binding to β_2 AR and how G protein dissociation from the receptor
525 may commence in the nucleotide-free state. These questions are important for understanding the
526 activation of GPCRs and their modulation by G protein interactions in normal physiological and
527 pathophysiological conditions. Our results can also be used to inform the next generation of
528 multiscale functional kinetic models of sympathetic nervous stimulation in cardiac myocytes and
529 other excitable cells, which is a powerful tool to complement experimental and clinical research.

530

531

532 **Materials and Methods**

533

534 Protein structures

535 The 3D coordinates of adrenaline-bound β_2 AR were obtained from the published X-ray
536 crystallographic structure (PDB: 4LDO) (59) to serve as a template for the activated receptor. The
537 G_s heterotrimer template was obtained from the 3D coordinates of the crystal structure of β_2 AR-
538 G_s complex (PDB: 3SN6) bound to agonist BI-167107 (P0G) (7). 3D coordinates were oriented
539 via the Orientations of Proteins in Membranes (OPM) database (60). The adrenaline-bound
540 receptor from PDB 4LDO was aligned to protein complex structure from PDB 3SN6 via UCSF
541 Chimera (61) Matchmaker to replace the P0G-bound receptor of PDB 3SN6, then all ligands and
542 non-physiological proteins were removed. The resulting template, which combined the receptor of
543 4LDO with the G_s heterotrimer of 3SN6, was then assessed for clashing van der Waals radii
544 before proceeding.

545 As the β_2 AR structure was published without 3D coordinates for the intracellular loop 3 (ICL3),
546 this region as well as omitted regions of the published G_s model in PDB 3SN6 were remodeled
547 using the ROSETTA implementation of fragment-based cyclic coordinate descent (CCD) (62, 63).
548 Target sequences for *de novo* modeling of both the human β_2 AR and the G_s heterotrimer were
549 obtained via UniProt (64). Rosetta comparative modeling (RosettaCM) was used with the Rosetta
550 Membrane Energy Function to generate 10,000 decoy models of sequence-complete β_2 AR- G_s
551 complex (65-67). Rosetta clustering analysis was used to assess convergence of decoys into
552 different microstates using their RMSDs with a cluster radius of 2.5 Å. The lowest-energy decoy
553 of the most populated cluster was selected as a model for further refinement. 1,000 energy-
554 minimized decoys were then generated from the sequence-complete model using the Rosetta
555 Fast Relax application in conjunction with the membrane energy function (68). Relaxation was
556 permitted only to residues that were modeled *de novo*. The lowest energy structure was then
557 selected for ligand docking and MD simulations.

558 Ligand docking

559 RosettaLigand (69) was used for all docking simulations of NE(+) to β_2 AR and β_2 AR- G_s . Ligand
560 rotamers and parameters were generated by OpenEye Omega (70) and ROSETTA scripts. A box
561 size of 5 Å was used for ligand transformations along with 7 Å ligand distance cutoff for side chain
562 and backbone reorientations (with <0.3 Å C_α restraint). 50,000 structures were generated in each
563 run with top 10% selected by total score, out of which 50 lowest-interfacial score structures were
564 validated for their convergence with the crystalized adrenaline of the original template structure
565 4LDO. Subsequent simulations were conducted using the lowest-interfacial score structures.

566 Molecular dynamics simulations

567 MD simulation systems of ~222,000 or ~302,000 atoms were generated using CHARMM-GUI
568 (71-73) and consisted of β_2 AR protein or β_2 AR-G_s protein complex in lipid bilayers soaked by a
569 0.15 M NaCl aqueous solution. The outer bilayer leaflet contained pure 1-Palmitoyl-2-
570 oleoylphosphatidylcholine (POPC) whereas the inner leaflet had ~70% POPC and ~30% 1-
571 Palmitoyl-2-oleoylphosphatidylserine (POPS) as in a previous MD simulation study (23). The
572 same ionizable protein residue protonation states, post-translational modifications (lipidations and
573 disulfide bonds based on UniProt data) and C- and N- protein termini as in that study (23) were
574 used as well. All-atom biomolecular CHARMM36m protein (74), C36 lipid (75) and general
575 CHARMM (CGENFF) (76) force field and TIP3P water (77) were used. CGENFF program (78,
576 79) was used to generate cationic norepinephrine, NE(+), force field parameters by analogy,
577 which were validated and had to be optimized for one dihedral angle using an established
578 quantum-mechanics (QM) based protocol (76).

579 MD simulations were run in the *NPT* ensemble at 310 K and 1 atm pressure using tetragonal
580 periodic boundary condition. The systems were equilibrated for 90 ns with gradually reducing
581 protein restraints in the first 40 ns using NAMD (80). MD equilibration runs were then followed by
582 multi-microsecond long production runs on the Anton 2 (81) supercomputer or using enhanced
583 sampling Gaussian accelerated MD (GaMD) (57) runs, respectively. The GaMD module
584 implemented in the NAMD (82) was applied to perform GaMD simulations, which included a 10-
585 ns short conventional MD (cMD) simulation (after the previous 90 ns MD equilibration), used to
586 collect potential statistics for calculating the GaMD acceleration parameters, 50-ns GaMD
587 equilibration after adding the boost potential, and finally three independent GaMD production runs
588 with randomized initial atomic velocities for each system. All GaMD simulations were run at the
589 “dual-boost” level by setting the reference energy to the lower bound. The upper limit of the boost
590 potential standard deviation (SD), σ_0 was set to 6.0 kcal/mol for both the dihedral and the total
591 potential energy terms. Simulation analyses were performed using VMD (50) and lab generated
592 codes. The PyReweighting toolkit (83) was used to reweight the PMF profiles based on the
593 distances and angles for GaMD trajectories to account for the effect of the boost potential on
594 GaMD simulated distributions. A bin size of 0.5 Å was used for the interatomic distances and 5°
595 for angles. The cutoff was set to 10 configurations in one bin for 2D PMF calculations. For the
596 Anton simulations, PMF profiles did not need to be reweighted.

597 **MM-PBSA binding energies**

598 Free energy calculations for β_2 AR-NE(+) binding and β_2 AR-G_s binding were performed using the
599 Molecular Mechanics Poisson-Boltzmann Surface Area (MM-PBSA) approach with all-atom MD
600 simulation trajectories by MMPBSA.py program in Amber Tools (84). The Chamber module of
601 ParmEd program was used to convert CHARMM-style forcefields to Amber-style forcefields (85).
602 Aqueous solution (ionic strength 150 mM) and lipid membrane were treated implicitly using
603 dielectric constants (water ϵ_w =80, lipid bilayer ϵ_l =2 and protein ϵ_p =4). Solvent probe radius is set
604 to 1.4 Å and the atomic radii were set according to the converted force field parameters. To
605 obtain the enthalpy (ΔH) contributions of solvation and gas-phase free energies, the particle-
606 particle particle-mesh (P3M) procedure was used (86). These calculations were performed with
607 implicit membrane, where the electrostatic energy includes both reaction field and Coulombic
608 electrostatic energies. Entropy was calculated separately by the interaction entropy method (87).
609 This method was shown to increase the entropy calculation efficiency and possibly improve the
610 accuracy of MM-PBSA in estimating protein-protein interactions (88). To use the interaction
611 entropy method, gas-phase interaction energies including Coulombic electrostatic and van der
612 Waals components were computed. In order to get the gas-phase Coulombic energy separated
613 from the reaction field energy contribution, each system energy was recalculated by using
614 dielectric boundary surface charges method in the implicit ionic solution. In this study we focused
615 on trends in relative binding free energies for the same or similar (β_2 AR and β_2 AR-G_s) protein
616 systems, which may justify usage of a standard MM-PBSA approach (84) along with interaction
617 entropy calculations (87). However, to obtain more accurate absolute and relative protein-protein

618 binding free energy estimates we may need to use recently developed MM-PBSA method with a
619 screened electrostatic energy (88) in subsequent studies.

620 To reweight the MM-PBSA energies computed from GaMD simulations, we used the
621 PyReweighting toolkit (83) to generate a corresponding PMF (W) value for each bin of the energy
622 histogram generated from the simulation trajectories as described above for distance and angle
623 PMFs. The probability for each bin can then be computed as $P_{bin} = e^{-\beta W}$, where $\beta = 1/(k_B T)$, k_B
624 is Boltzmann constant and T is temperature. The average MM-PBSA energy in the GaMD boost-
625 potential biased ensemble (notated with an asterisk, $\langle E^* \rangle$) is then converted to the canonical
626 ensemble value $\langle E \rangle$ using probabilities, P_{bin} , and energies, E_{bin}^* , for each bin as $\langle E \rangle =$
627 $\frac{\sum_{bin=1}^N P_{bin} E_{bin}^*}{\sum_{bin=1}^N P_{bin}}$. The bin width was kept as 0.5 kcal/mol. Similar reweighting approach can be in
628 principle applied to interaction entropies using e.g., a cumulant expansion approach outlined in
629 (89), but results for our systems were found to be noisy and unreliable (divergent) due to
630 domination of higher order terms.

631 Binding pose clustering

632 The clustering for the NE(+) binding poses was performed by TTClust program (90). The
633 trajectories were first aligned to the first frame of β_2 AR (without intracellular loop 3). The RMSDs
634 of NE(+) between all pairs of frames was calculated and stored into a matrix. This matrix was
635 then used to calculate a linkage matrix by the hierarchical cluster linkage function of the SciPy
636 package (91). Ward's method within the SciPy module was used to minimize the variance within
637 clusters and allows more demarcated clusters to be obtained (90). K-means clustering with the
638 Elbow algorithm was used to find the optimal number of clusters (90).

639 Pearson correlation coefficients

640 The Pearson correlation coefficients (values of r) shown in Table S4 were calculated among the
641 data points in Figures 4A and 4B collected from the average values of the last 2 μ s of each Anton
642 run.

643 The time-lag correlation analysis was performed using MATLAB version 2022b. Calculations of
644 the Pearson correlation coefficients (values of r) were performed using the built-in *corrcoef*
645 function. The lag time defines a delay between two different MD simulation measurements, e.g.,
646 the distance between two protein residues as compared to the angle between two protein
647 domains. A lag time of zero indicates that the distance and angle observations are compared
648 from the same simulation time points, whereas a lag time of 50 ns, for example, indicates that
649 distance observations for time t will be compared with angle observations from time ($t+50$) for the
650 duration of the simulation. The lag time was varied from zero to half of the MD simulation length
651 (e.g., 2.5 μ s for a 5 μ s long simulation).

652
653 **Acknowledgments**

654
655 We would like to thank Khoa Ngo and other members of the C.E.C. and V.Y.-Y. laboratories for
656 helpful discussions as well as Prof. Yinglong Miao and his group members for help with the setup
657 of GaMD simulations and their analyses. This work was supported by National Institutes of Health
658 Common Fund Grant OT2OD026580 (to C.E.C. and I.V.), National Heart, Lung, and Blood
659 Institute (NHLBI) grants R01HL128537, R01HL152681, and U01HL126273 (to C.E.C., V.Y.-Y.
660 and I.V.), NHLBI grant R01HL162825 and VA Merit grants 01BX005100 and IK6BX005753 (to
661 Y.K.X.), American Heart Association Predoctoral Fellowship grant 16PRE27260295 (to K.R.D.),
662 American Heart Association Career Development Award grant 19CDA34770101 (to I.V.),
663 National Science Foundation travel grant 2032486 (to I.V.), UC Davis Department of Physiology
664 and Membrane Biology Research Partnership Fund (to C.E.C. and I.V.) as well as UC Davis T32

665 Predoctoral Training in Pharmacological Sciences fellowship supported in part by NHLBI
666 Institutional Training Grant T32GM099608 (to J.R.D.D.) and UC Davis Chemical Biology Program
667 fellowship supported in part by National Institute of General Medical Sciences (NIGMS)
668 Institutional Training Grant 5T32GM136597-02 (to K.C.R.). Computer allocations were provided
669 through Extreme Science and Engineering Discovery Environment (XSEDE) grant MCB170095
670 (to I.V., C.E.C., V.Y.-Y. and K.R.D.), National Center for Supercomputing Applications (NCSA)
671 Blue Waters Broadening Participation Allocation (to C.E.C., I.V., K.R.D.), Texas Advanced
672 Computing Center (TACC) Leadership Resource and Pathways Allocations MCB20010 (I.V.,
673 C.E.C., V.Y.-Y., and K.R.D.), Oracle cloud credits award (to I.V., C.E.C.), Pittsburgh
674 Supercomputing Center (PSC) Anton 2 allocations PSCA17085P, MCB160089P, PSCA18077P,
675 PSCA17085P, PSCA16108P (to I.V., C.E.C., V.Y.-Y. and K.R.D.). Anton 2 computer time was
676 provided by the Pittsburgh Supercomputing Center (PSC) through Grant R01GM116961 from the
677 National Institutes of Health. The Anton 2 machine (70) at PSC was generously made available
678 by D.E. Shaw Research.

679

680

681

682 **Figure captions**

683

684

685 **Figure 1.** NE(+) bound β_2 AR coupled with G_s protein. Different subunits and loops are illustrated
686 by different colors (Green – β_2 AR, Gray –intracellular loop 3 or ICL3, Pink – $G_s\alpha$ AH domain, Red
687 – $G_s\alpha$ Ras domain, Blue – $G\beta$, Yellow – $G\gamma$).

688

689 **Figure 2.** NE(+) binding poses and time series of center-to-center distances between NE(+) and
690 β_2 AR. (A) The initial (gray) and three special representative binding poses of NE(+) found in β_2 AR
691 (cluster 4 – in magenta) and β_2 AR- G_s (cluster 4 – in light-blue and cluster 5 – in red) systems.
692 See Figure S1 for binding pose clustering information (B) Time series for center-to-center
693 distances between NE(+) and β_2 AR (without intracellular loops) with the three special poses in
694 panel A matching the plot colors. (C) The initial and dominant NE(+) binding pose and interacting
695 β_2 AR residues. C atoms are shown in gray for NE(+) and in cyan for residues of β_2 AR, O atoms
696 are in red, N atoms are in blue, H atoms are omitted. H-bonds between NE(+) and β_2 AR residues
697 S203^{5,42}, N312^{7,39} and D113^{3,32} are shown as dashed lines. (D) The special representative binding
698 pose of NE(+) found in β_2 AR system cluster 4 (magenta) and interacting β_2 AR residues. H-bonds
699 between the NE(+) and N312^{7,39}, D113^{3,32} are shown as dashed lines. The preserved residues
700 from the initial binding pocket in panel C are shown with cyan C atoms, whereas new residues in
701 the binding pocket are shown with gray C atoms. (E) The special representative NE(+) binding
702 pose from β_2 AR- G_s cluster 4 (light blue) and interacting β_2 AR residues in the binding pocket,
703 which follow the same rendering style as in panel D. The geometric centers were used for the
704 distance measurements. The Ballesteros-Weinstein (BW) numbering for the residues can be
705 found in the text and is omitted in the figure for clarity.

706 **Figure 3.** All-atom MD simulations of the active state human β_2 AR- G_s with NE(+) bound based on
707 Anton runs. (A) run 1 with the top inset. (B) run 2 with the bottom inset. Final structures are
708 captured from the 5 μ s long unbiased MD simulation runs. Individual protein chains / subunits are
709 labeled and shown in the ribbon representation using different colors. $G_s\alpha$ α 5 helix and β_2 AR
710 intracellular loop 3 (ICL3) are colored in yellow and gray. C α atoms of residues A161 on $G_s\alpha$ AH
711 domain and E299 on $G_s\alpha$ Ras domain are shown as blue and green balls, and distances between
712 them are shown by light-blue dashed arrows. The quantification of the interactions between ICL3
713 and α 5 helix can be found in Table S3. The geometric centers were used for the distance
714 measurements. The common $G\alpha$ numbering (CGN) numbers (D381^{G,H5,13}, D378^{G,H5,10}, N377^{G,H5,9},
715 R374^{G,H5,6}, R385^{G,H5,17}) for residues in $G_s\alpha$ α 5 as well as A161^{H,HD,5} and E299^{G,HG,6} are omitted in
716 the figure for clarity.

717 **Figure 4.** Analysis of $G_s\alpha$ conformation and its possible partial dissociation from β_2 AR based on
718 all-atom MD Anton runs. The distances and angle shown in each run are based on their average
719 values during the last 2 μ s of MD simulations. The distances and angles were measured between
720 geometric centers of protein residues or domains. (A) A161–E299 distances indicating $G_s\alpha$ protein
721 conformational change (opening or closing), $G_s\alpha$ AH– $G_s\alpha$ Ras distances indicating relative
722 movement between the two domains, the angle between the two vectors of $G_s\alpha$ AH and $G_s\alpha$ Ras
723 domains indicating their relative orientation (B) α 1 – α 5 distances indicating relative movement
724 between α 1 and α 5 helices in $G_s\alpha$, β_2 AR – α 5 distances indicating possible partial dissociation of
725 $G_s\alpha$ α 5 helix from the receptor, and β_2 AR NPxxY motif – α 5 helix distances also indicating $G_s\alpha$ α 5
726 partial dissociation. (C) Illustration of the angle between $G_s\alpha$ AH and $G_s\alpha$ Ras domains; vector 1
727 goes through $G_s\alpha$ AH and A161 centers; vector 2 goes through $G_s\alpha$ Ras and E299 centers. (D)
728 Illustrations of $G_s\alpha$ α 5 helix (yellow), α 1 helix (cyan), and β_2 AR NPxxY motif (blue helix on
729 transmembrane domain 7).

730 **Figure 5.** 2D potential of mean force (PMF) or free energy profiles (in kcal/mol) based on $G_s\alpha$
731 conformation and its possible partial dissociation from β_2 AR based on all-atom Anton MD

732 simulations of the active state of the human β_2 AR-G_s complexes with NE(+). The 0.5 kcal/mol
733 contour lines are shown as bold black curves. Relative free energy values from 0 to 8 kcal/mol
734 are indicated by different colors from blue to red. All distances were measured between
735 geometric centers of protein residues or domains. (A) A161 – E299 distance indicating G_s α
736 opening or closing is shown as X axis; distance between G_s α α 5 and β_2 AR indicating possible
737 partial G_s dissociation is shown as Y axis. (B) G_s α α 1 – α 5 distance is shown as X axis; distance
738 between G_s α α 5 and β_2 AR is shown as Y axis. The contour lines are smoothed for better
739 visualization.

740

741 **References**

742 1. M. N. Alshak, J. M. Das, *Neuroanatomy, Sympathetic Nervous System* (StatPearls
743 Publishing, Treasure Island (FL), 2021).

744 2. A. Lymeropoulos, G. Rengo, W. J. Koch, Adrenergic nervous system in heart failure:
745 pathophysiology and therapy. *Circ. Res.* **113**, 739-753 (2013).

746 3. D. B. Bylund *et al.*, International Union of Pharmacology nomenclature of adrenoceptors.
747 *Pharmacol. Rev.* **46**, 121-136 (1994).

748 4. S. B. Wachter, E. M. Gilbert, Beta-adrenergic receptors, from their discovery and
749 characterization through their manipulation to beneficial clinical application. *Cardiology*
750 **122**, 104-112 (2012).

751 5. D. Goricanec *et al.*, Conformational dynamics of a G-protein alpha subunit is tightly
752 regulated by nucleotide binding. *Proc. Natl. Acad. Sci. U.S.A.* **113**, E3629-3638 (2016).

753 6. X. Liu *et al.*, Structural Insights into the Process of GPCR-G Protein Complex Formation.
754 *Cell* **177**, 1243-1251 e1212 (2019).

755 7. S. G. Rasmussen *et al.*, Crystal structure of the beta2 adrenergic receptor-Gs protein
756 complex. *Nature* **477**, 549-555 (2011).

757 8. M. Su *et al.*, Structural Basis of the Activation of Heterotrimeric Gs-Protein by
758 Isoproterenol-Bound beta1-Adrenergic Receptor. *Mol. Cell* **80**, 59-71 e54 (2020).

759 9. R. K. Sunahara, J. J. G. Tesmer, A. G. Gilman, S. R. Sprang, Crystal Structure of the
760 Adenylyl Cyclase Activator Gsa. *Science* **278**, 1943-1947 (1997).

761 10. R. O. Dror *et al.*, Identification of two distinct inactive conformations of the β 2-
762 adrenergic receptor reconciles structural and biochemical observations. *Proc. Natl. Acad.
763 Sci. U.S.A.* **106**, 4689-4694 (2009).

764 11. S. Vanni, M. Neri, I. Tavernelli, U. Rothlisberger, Observation of “ionic lock” formation in
765 molecular dynamics simulations of wild-type β 1 and β 2 adrenergic receptors.
766 *Biochemistry* **48**, 4789-4797 (2009).

767 12. R. O. Dror *et al.*, Activation mechanism of the β 2-adrenergic receptor. *Proc. Natl. Acad.
768 Sci. U.S.A.* **108**, 18684-18689 (2011).

769 13. R. Nygaard *et al.*, The dynamic process of β 2-adrenergic receptor activation. *Cell* **152**,
770 532-542 (2013).

771 14. M. I. Mahmood, X. Liu, S. Neya, T. Hoshino, Influence of lipid composition on the
772 structural stability of g-protein coupled receptor. *Chem. Pharm. Bull.* **61**, 426-437 (2013).

773 15. O. Ozcan, A. Uyar, P. Doruker, E. D. Akten, Effect of intracellular loop 3 on intrinsic
774 dynamics of human β 2-adrenergic receptor. *BMC Struct. Biol.* **13**, 1-17 (2013).

775 16. C. Neale, H. D. Herce, R. Pomès, A. E. García, Can specific protein-lipid interactions
776 stabilize an active state of the beta 2 adrenergic receptor? *Biophys. J.* **109**, 1652-1662
777 (2015).

778 17. O. Fleetwood, P. Matricon, J. Carlsson, L. Delemotte, Energy landscapes reveal agonist
779 control of G protein-coupled receptor activation via microswitches. *Biochemistry* **59**,
780 880-891 (2020).

781 18. A. Goetz, H. Lanig, P. Gmeiner, T. Clark, Molecular dynamics simulations of the effect of
782 the G-protein and diffusible ligands on the β 2-adrenergic receptor. *J. Mol. Biol.* **414**,
783 611-623 (2011).

784 19. Z. Feng, T. Hou, Y. Li, Studies on the interactions between β 2 adrenergic receptor and Gs
785 protein by molecular dynamics simulations. *J. Chem. Inf. Model* **52**, 1005-1014 (2012).

786 20. Q. Bai, Y. Zhang, Y. Ban, H. Liu, X. Yao, Computational study on the different ligands
787 induced conformation change of β 2 adrenergic receptor-Gs protein complex. *PLoS one* **8**,
788 e68138 (2013).

789 21. R. C. Kling, H. Lanig, T. Clark, P. Gmeiner, Active-state models of ternary GPCR complexes:
790 determinants of selective receptor-G-protein coupling. *PLoS one* **8**, e67244 (2013).

791 22. X. Sun, H. Ågren, Y. Tu, Microsecond molecular dynamics simulations provide insight
792 into the allosteric mechanism of the Gs protein uncoupling from the β 2 adrenergic
793 receptor. *J. Phys. Chem. B* **118**, 14737-14744 (2014).

794 23. R. O. Dror *et al.*, Structural basis for nucleotide exchange in heterotrimeric G proteins.
795 *Science* **348**, 1361-1365 (2015).

796 24. V. Kumar *et al.*, GDP Release from the Open Conformation of $\text{G}\alpha$ Requires Allosteric
797 Signaling from the Agonist-Bound Human β 2 Adrenergic Receptor. *J. Chem. Inf. Model.*
798 **60**, 4064-4075 (2020).

799 25. K. E. Komolov *et al.*, Structural and functional analysis of a β 2-adrenergic receptor
800 complex with GRK5. *Cell* **169**, 407-421. e416 (2017).

801 26. Y. Chen, O. Fleetwood, S. Pérez-Conesa, L. Delemotte, Allosteric Effect of Nanobody
802 Binding on Ligand-Specific Active States of the β 2 Adrenergic Receptor. *J. Chem. Inf.*
803 *Model.* **61**, 6024-6037 (2021).

804 27. L. Zhao, X. He, H. Jiang, X. Cheng, Computational characterization of transducer
805 recognition of β 2 adrenergic receptor. *Biochem. Biophys. Res. Commun.* **592**, 67-73
806 (2022).

807 28. T. Wang, Y. Duan, Ligand entry and exit pathways in the β 2-adrenergic receptor. *J. Mol.*
808 *Biol.* **392**, 1102-1115 (2009).

809 29. R. O. Dror *et al.*, Pathway and mechanism of drug binding to G-protein-coupled
810 receptors. *Proc. Natl. Acad. Sci. U.S.A.* **108**, 13118-13123 (2011).

811 30. A. González, T. Perez-Acle, L. Pardo, X. Deupi, Molecular basis of ligand dissociation in β -
812 adrenergic receptors. *PLoS one* **6**, e23815 (2011).

813 31. S. Vanni, M. Neri, I. Tavernelli, U. Rothlisberger, Predicting novel binding modes of
814 agonists to β adrenergic receptors using all-atom molecular dynamics simulations. *PLoS*
815 *Comput. Biol.* **7**, e1001053 (2011).

816 32. I. G. Tikhonova, B. Selvam, A. Ivetac, J. Wereszczynski, J. A. McCammon, Simulations of
817 biased agonists in the β 2 adrenergic receptor with accelerated molecular dynamics.
818 *Biochemistry* **52**, 5593-5603 (2013).

819 33. A. Plazinska, M. Kolinski, I. W. Wainer, K. Jozwiak, Molecular interactions between
820 fenoterol stereoisomers and derivatives and the β 2-adrenergic receptor binding site
821 studied by docking and molecular dynamics simulations. *J. Mol. Model.* **19**, 4919-4930
822 (2013).

823 34. A. Ranganathan, R. O. Dror, J. Carlsson, Insights into the role of Asp792. 50 in β 2
824 adrenergic receptor activation from molecular dynamics simulations. *Biochemistry* **53**,
825 7283-7296 (2014).

826 35. A. Tandale, M. Joshi, D. Sengupta, Structural insights and functional implications of
827 inter-individual variability in β 2-adrenergic receptor. *Sci. Rep.* **6**, 1-11 (2016).

828 36. A. Plazinska, W. Plazinski, Stereoselective binding of agonists to the β 2-adrenergic
829 receptor: insights into molecular details and thermodynamics from molecular dynamics
830 simulations. *Mol. Biosyst.* **13**, 910-920 (2017).

831 37. J. Wang, Y. Miao, Recent advances in computational studies of GPCR-G protein
832 interactions. *Adv. Protein Chem. Struct. Biol.* **116**, 397-419 (2019).

833 38. D. Hilger, The role of structural dynamics in GPCR - mediated signaling. *FEBS J.* **288**,
834 2461-2489 (2021).

835 39. J. M. L. Ribeiro, M. Filizola, Allostery in G protein-coupled receptors investigated by
836 molecular dynamics simulations. *Curr. Opin. Struct. Biol.* **55**, 121-128 (2019).

837 40. R. Alhadeff, I. Vorobyov, H. W. Yoon, A. Warshel, Exploring the free-energy landscape of
838 GPCR activation. *Proc. Natl. Acad. Sci. U.S.A.* **115**, 10327-10332 (2018).

839 41. C. Bai *et al.*, Exploring the Activation Process of the beta2AR-Gs Complex. *J. Am. Chem.
840 Soc.* **143**, 11044-11051 (2021).

841 42. D. Provasi, A. Bortolato, M. Filizola, Exploring molecular mechanisms of ligand
842 recognition by opioid receptors with metadynamics. *Biochemistry* **48**, 10020-10029
843 (2009).

844 43. S. Schneider, D. Provasi, M. Filizola, "The dynamic process of drug-GPCR binding at
845 either orthosteric or allosteric sites evaluated by metadynamics" in *G Protein-Coupled
846 Receptors in Drug Discovery*. (Springer, 2015), pp. 277-294.

847 44. N. Saleh, P. Ibrahim, G. Saladino, F. L. Gervasio, T. Clark, An efficient metadynamics-
848 based protocol to model the binding affinity and the transition state ensemble of G-
849 protein-coupled receptor ligands. *J. Chem. Inf. Model.* **57**, 1210-1217 (2017).

850 45. P. Ibrahim, T. Clark, Metadynamics simulations of ligand binding to GPCRs. *Curr. Opin.
851 Struct. Biol.* **55**, 129-137 (2019).

852 46. J. A. Ballesteros, H. Weinstein, *Integrated methods for the construction of three-
853 dimensional models and computational probing of structure-function relations in G
854 protein-coupled receptors* S. C. Sealfon, Ed., *Methods in neurosciences* (Academic Press,
855 1995), vol. 25, pp. 366-428.

856 47. Y. Miao, A. Bhattacharai, J. Wang, Ligand Gaussian Accelerated Molecular Dynamics
857 (LiGaMD): Characterization of Ligand Binding Thermodynamics and Kinetics. *J. Chem.
858 Theory Comput.* **16**, 5526-5547 (2020).

859 48. D. Guo *et al.*, Molecular Basis of Ligand Dissociation from the Adenosine A2A Receptor.
860 *Mol. Pharmacol.* **89**, 485-491 (2016).

861 49. Y. Miao, J. A. McCammon, Graded activation and free energy landscapes of a muscarinic
862 G-protein-coupled receptor. *Proc. Natl. Acad. Sci. U.S.A.* **113**, 12162-12167 (2016).

863 50. W. Humphrey, A. Dalke, K. Schulten, VMD - Visual Molecular Dynamics. *J. Mol. Graph.*
864 **14**, 33-38 (1996).

865 51. T. Flock *et al.*, Universal allosteric mechanism for Galphai activation by GPCRs. *Nature*
866 **524**, 173-179 (2015).

867 52. J. L. DeGraff, V. V. Gurevich, J. L. Benovic, The third intracellular loop of alpha 2-
868 adrenergic receptors determines subtype specificity of arrestin interaction. *J. Biol. Chem.*
869 **277**, 43247-43252 (2002).

870 53. K. O. Alegre *et al.*, Structural basis and mechanism of activation of two different families
871 of G proteins by the same GPCR. *Nat. Struct. Mol. Biol.* **28**, 936-944 (2021).

872 54. J. Wang, Y. Miao, Mechanistic Insights into Specific G Protein Interactions with
873 Adenosine Receptors. *J. Phys. Chem. B* **123**, 6462-6473 (2019).

874 55. K. J. Culhane, T. M. Gupte, I. Madhugiri, C. J. Gadgil, S. Sivaramakrishnan, Kinetic model
875 of GPCR-G protein interactions reveals allosteric modulation of signaling. *Nat. Commun.*
876 **13**, 1202 (2022).

877 56. D. Hilger, M. Masureel, B. K. Kobilka, Structure and dynamics of GPCR signaling
878 complexes. *Nat. Struct. Mol. Biol.* **25**, 4-12 (2018).

879 57. Y. Miao, V. A. Feher, J. A. McCammon, Gaussian Accelerated Molecular Dynamics:
880 Unconstrained Enhanced Sampling and Free Energy Calculation. *J. Chem. Theory Comput.*
881 **11**, 3584-3595 (2015).

882 58. J. Wang, Y. Miao, Protein–Protein Interaction-Gaussian Accelerated Molecular Dynamics
883 (PPI-GaMD): Characterization of Protein Binding Thermodynamics and Kinetics. *J. Chem.*
884 *Theory Comput.* **18**, 1275-1285 (2022).

885 59. A. M. Ring *et al.*, Adrenaline-activated structure of β 2-adrenoceptor stabilized by an
886 engineered nanobody. *Nature* **502**, 575-579 (2013).

887 60. M. A. Lomize, I. D. Pogozheva, H. Joo, H. I. Mosberg, A. L. Lomize, OPM database and
888 PPM web server: resources for positioning of proteins in membranes. *Nucleic Acids Res*
889 **40**, D370-D376 (2012).

890 61. E. F. Pettersen *et al.*, UCSF Chimera--a visualization system for exploratory research and
891 analysis. *J. Comput. Chem.* **25**, 1605-1612 (2004).

892 62. C. Wang, P. Bradley, D. Baker, Protein-protein docking with backbone flexibility. *J. Mol.*
893 *Biol.* **373**, 503-519 (2007).

894 63. A. A. Canutescu, R. L. Dunbrack, Jr., Cyclic coordinate descent: A robotics algorithm for
895 protein loop closure. *Protein Sci.* **12**, 963-972 (2003).

896 64. T. U. Consortium, UniProt: the universal protein knowledgebase in 2021. *Nucleic Acids*
897 *Res* **49**, D480-D489 (2020).

898 65. Y. Song *et al.*, High-resolution comparative modeling with RosettaCM. *Structure* **21**,
899 1735-1742 (2013).

900 66. V. Yarov-Yarovoy, J. Schonbrun, D. Baker, Multipass membrane protein structure
901 prediction using Rosetta. *Proteins* **62**, 1010-1025 (2006).

902 67. R. F. Alford *et al.*, The Rosetta All-Atom Energy Function for Macromolecular Modeling
903 and Design. *J. Chem. Theory Comput.* **13**, 3031-3048 (2017).

904 68. P. Conway, M. D. Tyka, F. DiMaio, D. E. Konnerding, D. Baker, Relaxation of backbone
905 bond geometry improves protein energy landscape modeling. *Protein Sci.* **23**, 47-55
906 (2014).

907 69. J. Meiler, D. Baker, ROSETTALIGAND: protein-small molecule docking with full side-chain
908 flexibility. *Proteins* **65**, 538-548 (2006).

909 70. P. C. D. Hawkins, A. G. Skillman, G. L. Warren, B. A. Ellingson, M. T. Stahl, Conformer
910 Generation with OMEGA: Algorithm and Validation Using High Quality Structures from
911 the Protein Databank and Cambridge Structural Database. *J. Chem. Inf. Model.* **50**, 572-
912 584 (2010).

913 71. J. Lee *et al.*, CHARMM-GUI Input Generator for NAMD, GROMACS, AMBER, OpenMM,
914 and CHARMM/OpenMM Simulations Using the CHARMM36 Additive Force Field. *J.*
915 *Chem. Theory Comput.* **12**, 405-413 (2016).

916 72. B. R. Brooks *et al.*, CHARMM: the biomolecular simulation program. *J. Comput. Chem.* **30**,
917 1545-1614 (2009).

918 73. S. Jo, T. Kim, V. G. Iyer, W. Im, CHARMM-GUI: a web-based graphical user interface for
919 CHARMM. *J. Comput. Chem.* **29**, 1859-1865 (2008).

920 74. J. Huang *et al.*, CHARMM36m: an improved force field for folded and intrinsically
921 disordered proteins. *Nat. Methods* **14**, 71 (2017).

922 75. J. B. Klauda *et al.*, Update of the CHARMM all-atom additive force field for lipids:
923 validation on six lipid types. *J. Phys. Chem. B* **114**, 7830-7843 (2010).

924 76. K. Vanommeslaeghe *et al.*, CHARMM General Force Field: A Force field for Drug-Like
925 Molecules Compatible with the CHARMM All-Atom Additive Biological Force Field. *J.
926 Comput. Chem.* **31**, 671-690 (2010).

927 77. W. L. Jorgensen, J. Chandrasekhar, J. D. Madura, R. W. Impey, M. L. Klein, Comparison of
928 Simple Potential Functions for Simulating Liquid Water. *J. Chem. Phys.* **79**, 926-935
929 (1983).

930 78. K. Vanommeslaeghe, A. D. MacKerell Jr, Automation of the CHARMM General Force
931 Field (CGenFF) I: bond perception and atom typing. *J. Chem. Inf. Model.* **52**, 3144-3154
932 (2012).

933 79. K. Vanommeslaeghe, E. P. Raman, A. D. MacKerell, Automation of the CHARMM General
934 Force Field (CGenFF) II: Assignment of Bonded Parameters and Partial Atomic Charges. *J.
935 Chem. Inf. Model.* **52**, 3155-3168 (2012).

936 80. J. C. Phillips *et al.*, Scalable molecular dynamics with NAMD. *J. Comput. Chem.* **26**, 1781-
937 1802 (2005).

938 81. D. E. Shaw *et al.* (2014) Anton 2: Raising the Bar for Performance and Programmability in
939 a Special-Purpose Molecular Dynamics Supercomputer. in *SC '14: Proceedings of the
940 International Conference for High Performance Computing, Networking, Storage and
941 Analysis*, pp 41-53.

942 82. Y. T. Pang, Y. Miao, Y. Wang, J. A. McCammon, Gaussian Accelerated Molecular
943 Dynamics in NAMD. *J. Chem. Theory Comput.* **13**, 9-19 (2017).

944 83. Y. Miao *et al.*, Improved Reweighting of Accelerated Molecular Dynamics Simulations for
945 Free Energy Calculation. *J. Chem. Theory Comput.* **10**, 2677-2689 (2014).

946 84. B. R. Miller, 3rd *et al.*, MMPBSA.py: An Efficient Program for End-State Free Energy
947 Calculations. *J. Chem. Theory Comput.* **8**, 3314-3321 (2012).

948 85. M. R. Shirts *et al.*, Lessons learned from comparing molecular dynamics engines on the
949 SAMPL5 dataset. *bioRxiv* 10.1101/077248, 077248 (2016).

950 86. Q. Lu, R. Luo, A Poisson-Boltzmann dynamics method with nonperiodic boundary
951 condition. *J. Chem. Phys.* **119**, 11035-11047 (2003).

952 87. L. Duan, X. Liu, J. Z. Zhang, Interaction Entropy: A New Paradigm for Highly Efficient and
953 Reliable Computation of Protein-Ligand Binding Free Energy. *J. Am. Chem. Soc.* **138**,
954 5722-5728 (2016).

955 88. Y. J. Sheng, Y. W. Yin, Y. Q. Ma, H. M. Ding, Improving the Performance of MM/PBSA in
956 Protein-Protein Interactions via the Screening Electrostatic Energy. *J. Chem. Inf. Model.*
957 **61**, 2454-2462 (2021).

958 89. W. M. Menzer, C. Li, W. Sun, B. Xie, D. D. Minh, Simple entropy terms for end-point
959 binding free energy calculations. *J. Chem. Theory Comput.* **14**, 6035-6049 (2018).

960 90. T. Tubiana, J. C. Carvaillo, Y. Boulard, S. Bressanelli, TTClust: A Versatile Molecular
961 Simulation Trajectory Clustering Program with Graphical Summaries. *J. Chem. Inf. Model.*
962 **58**, 2178-2182 (2018).

963 91. P. Virtanen *et al.*, SciPy 1.0: fundamental algorithms for scientific computing in Python.
964 *Nat. Methods* **17**, 261-272 (2020).

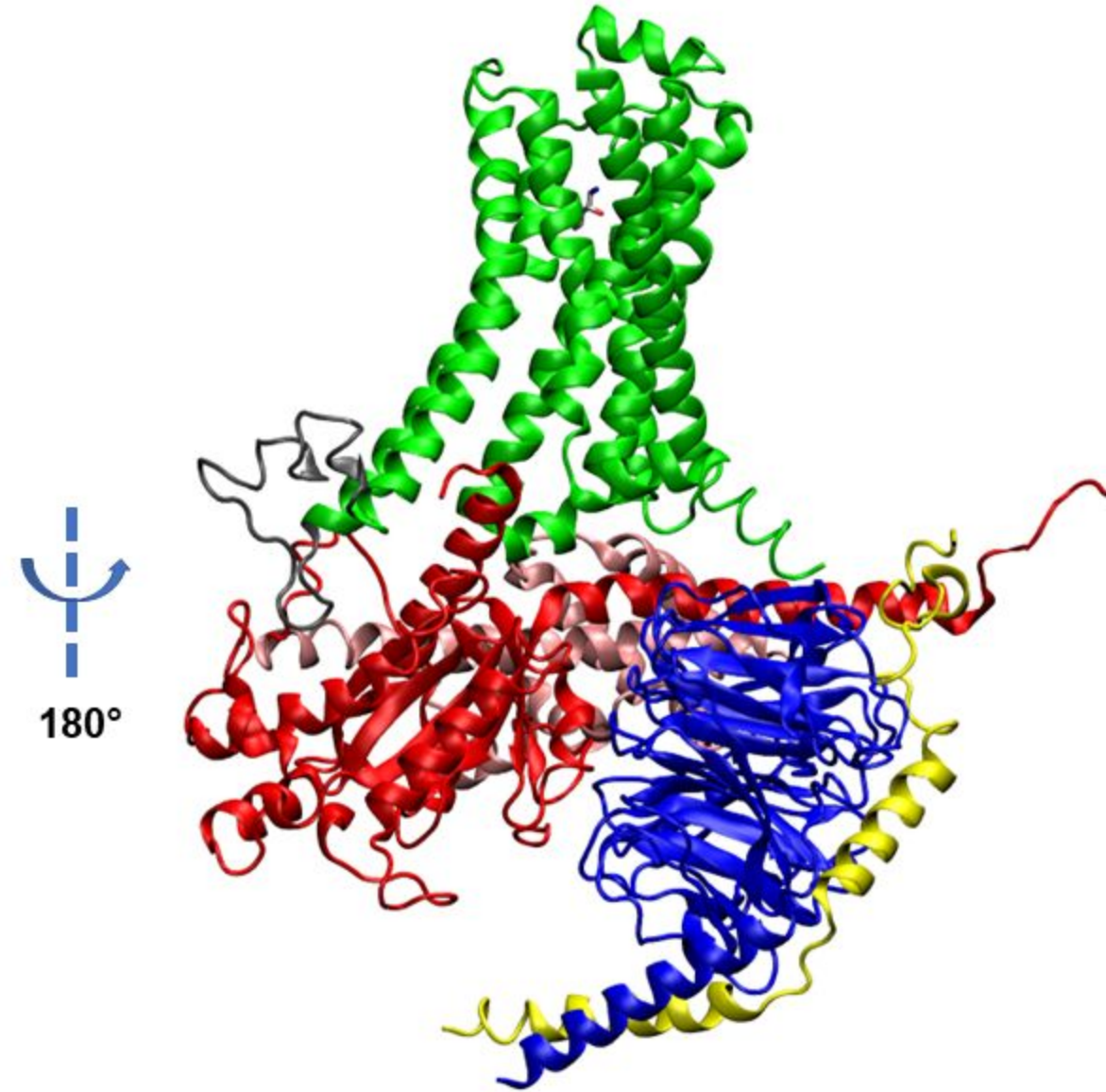
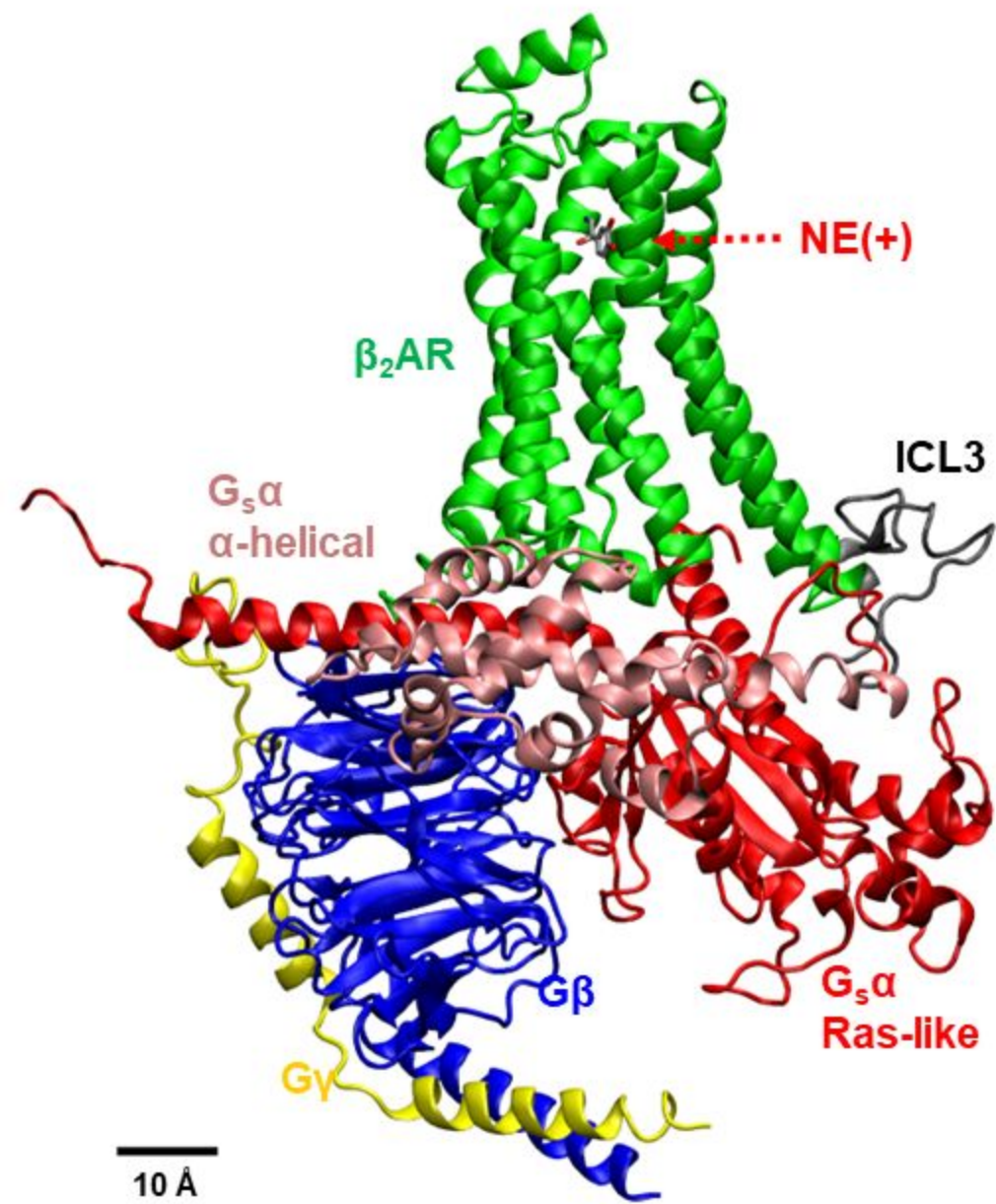
969
970
971

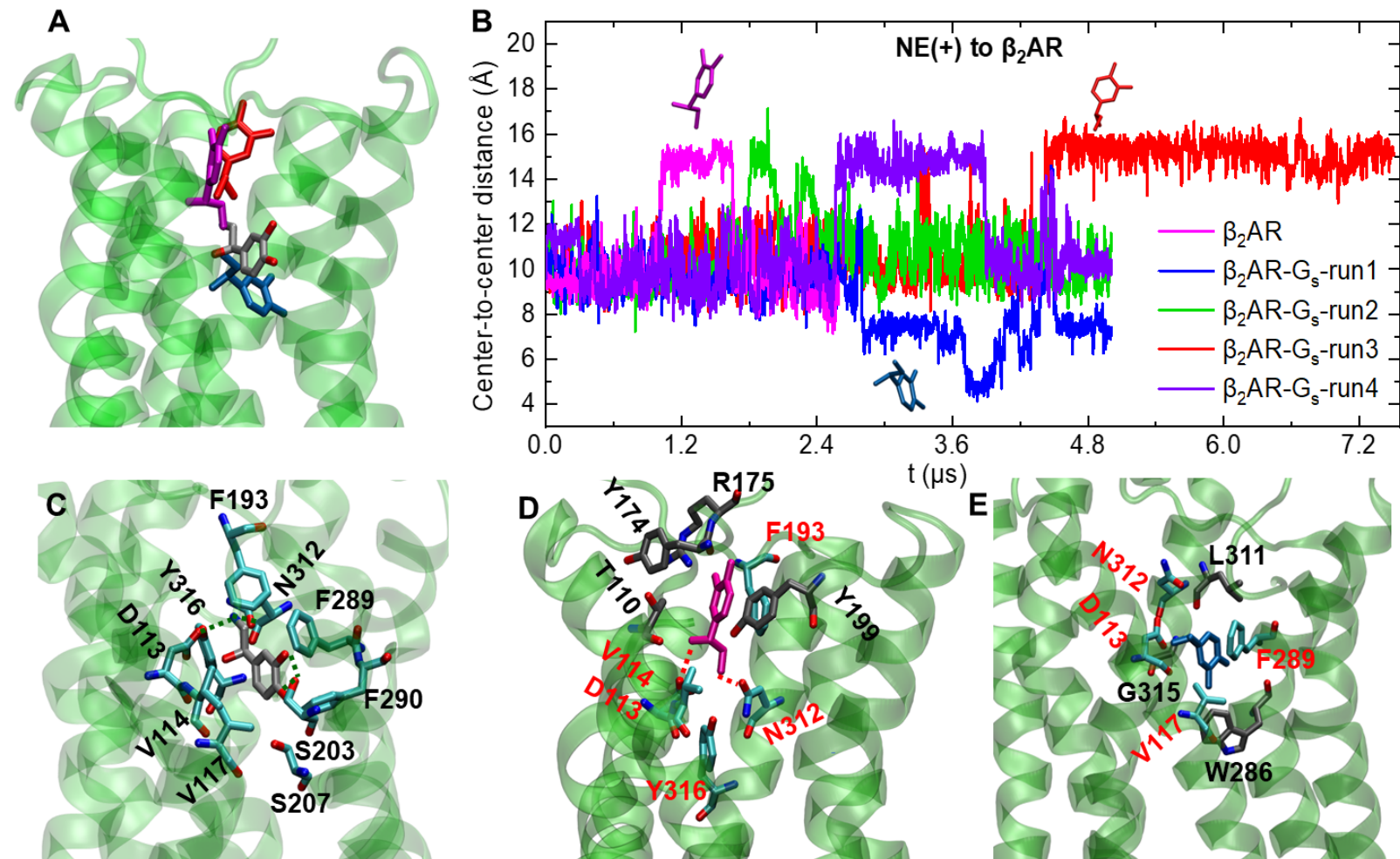
Table 1. MM-PBSA interaction free energies (ΔG) between NE(+) and β_2 AR (in kcal/mol) along with their standard errors of mean (SEM) computed using block averages, enthalpic (ΔH) and entropic ($-T\Delta S$) components as well as mean RMSD values (in Å) along with their standard deviations (SD) for β_2 AR without loops (the average structure was taken as reference; analysis was performed for the last 2 μ s of Anton trajectories). See also Figure S14 for analysis of correlations between MM-PBSA interaction energies, β_2 AR – NE(+) distances and RMSD values.

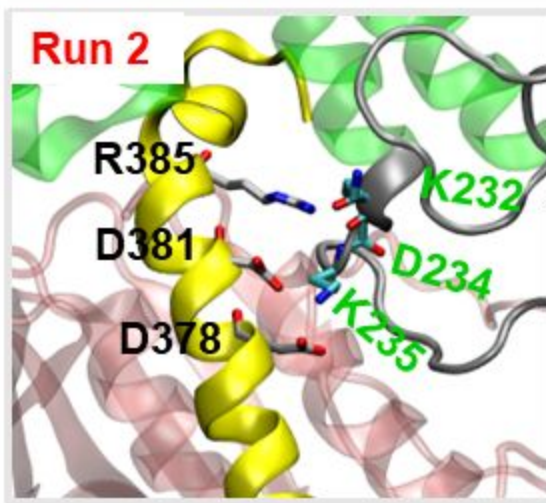
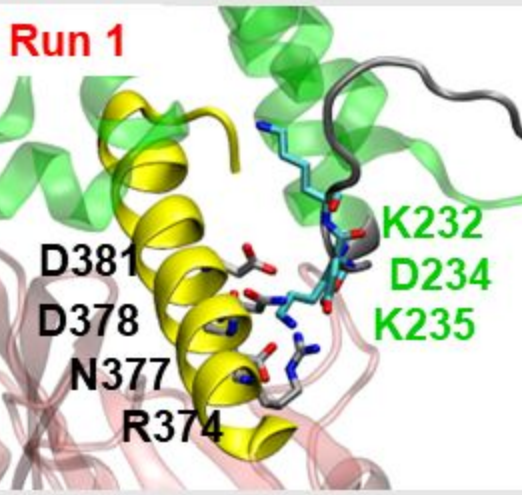
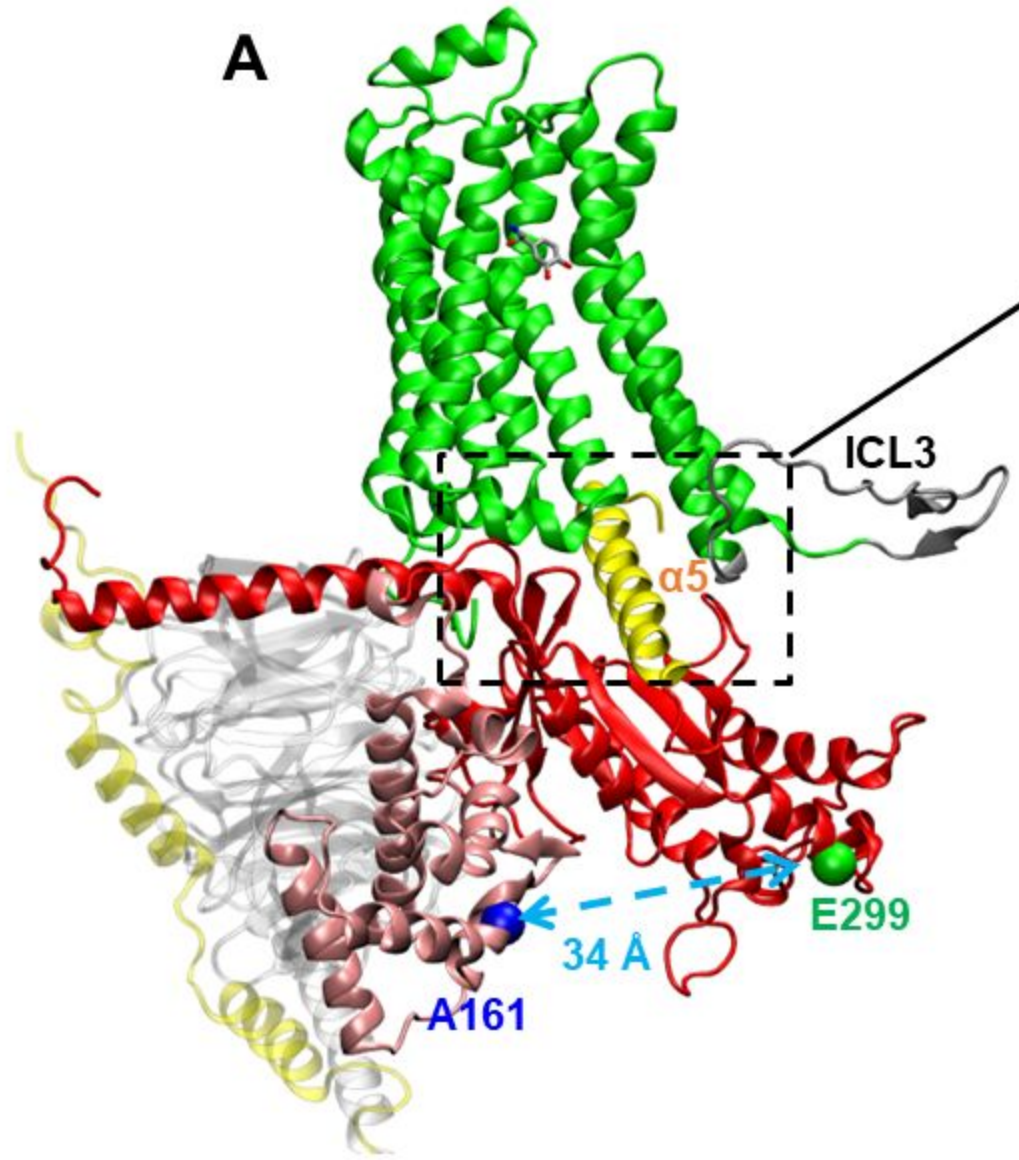
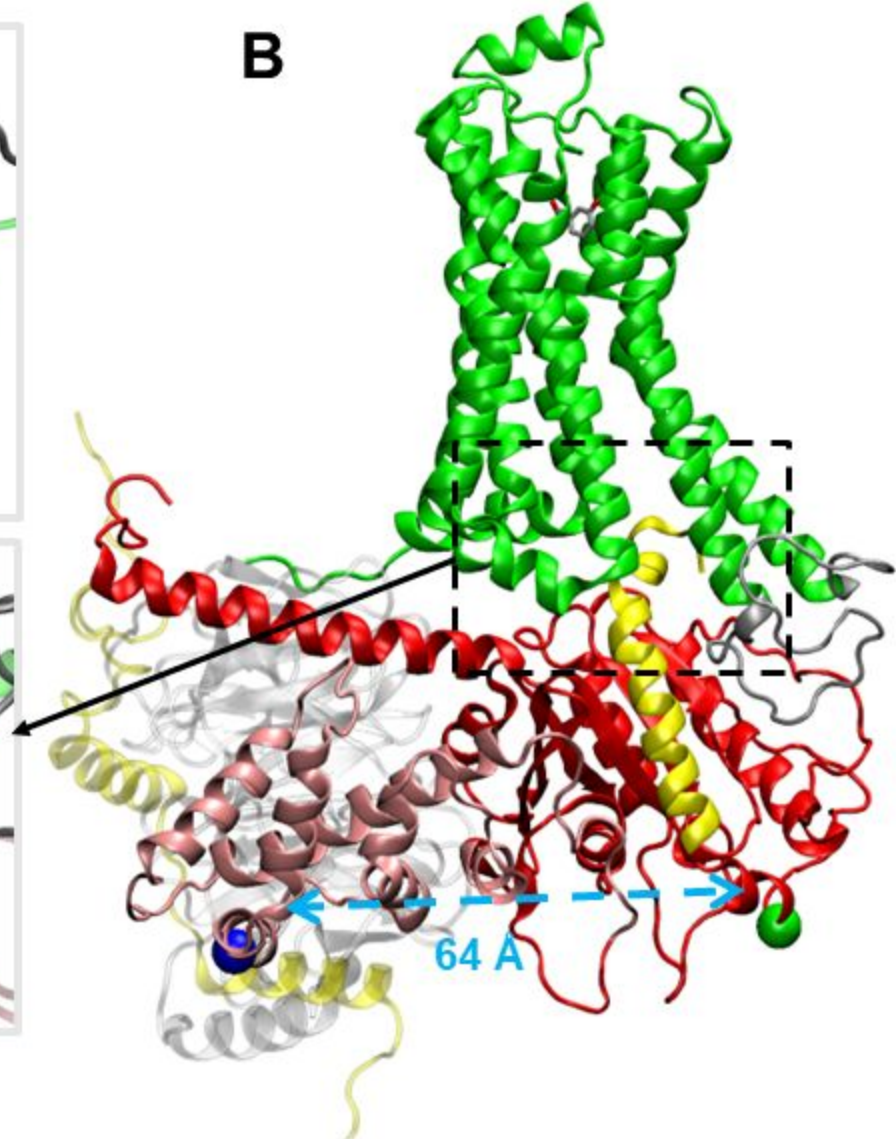
System	Time	ΔH	$-T\Delta S$	$\Delta G \pm SEM$	RMSD (SD)
β_2 AR	0.5 – 2.5 μ s	-21.61	6.88	-14.73 \pm 0.92	1.65 (0.26)
β_2 AR-G _s - run1	3.0 – 5.0 μ s	-27.54	11.92	-15.62 \pm 2.00	1.79 (0.23)
β_2 AR-G _s – run2	3.0 – 5.0 μ s	-25.09	6.10	-18.99 \pm 0.44	1.56 (0.21)
β_2 AR-G _s – run3	5.5 – 7.5 μ s	-23.70	7.91	-15.79 \pm 0.45	1.52 (0.15)
β_2 AR-G _s – run4	3.0 – 5.0 μ s	-22.42	10.81	-11.61 \pm 1.11	1.67 (0.16)

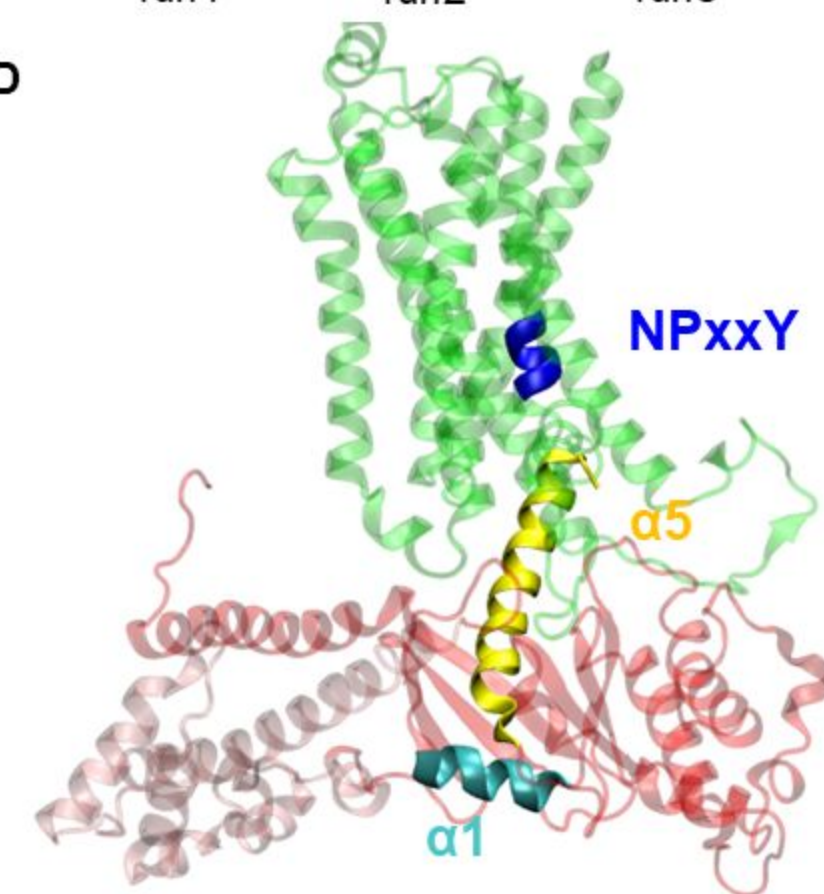
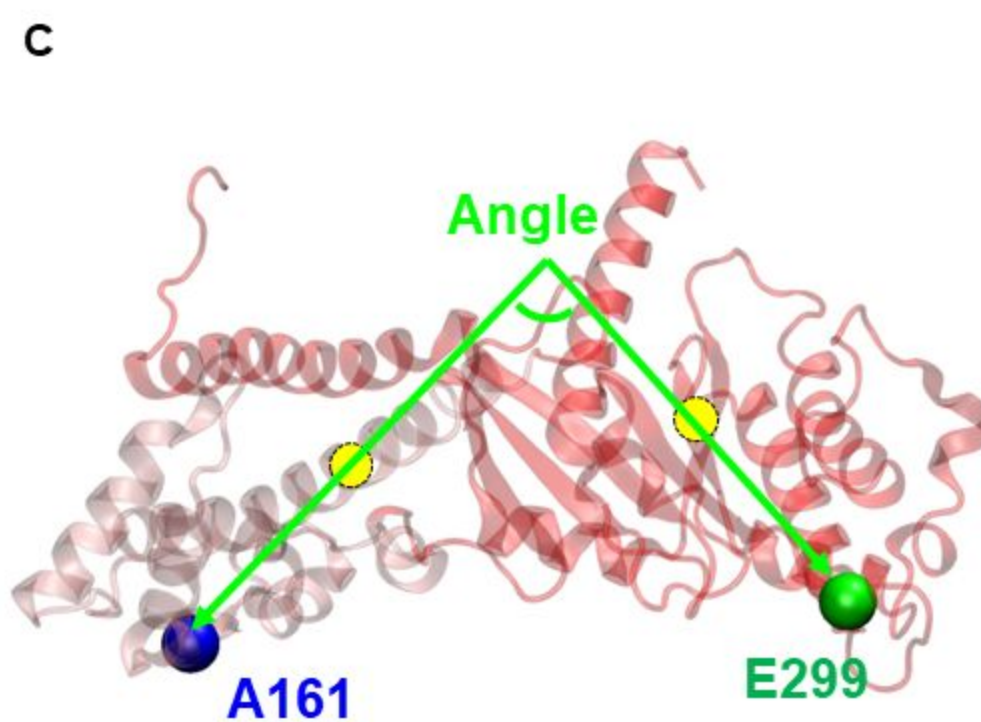
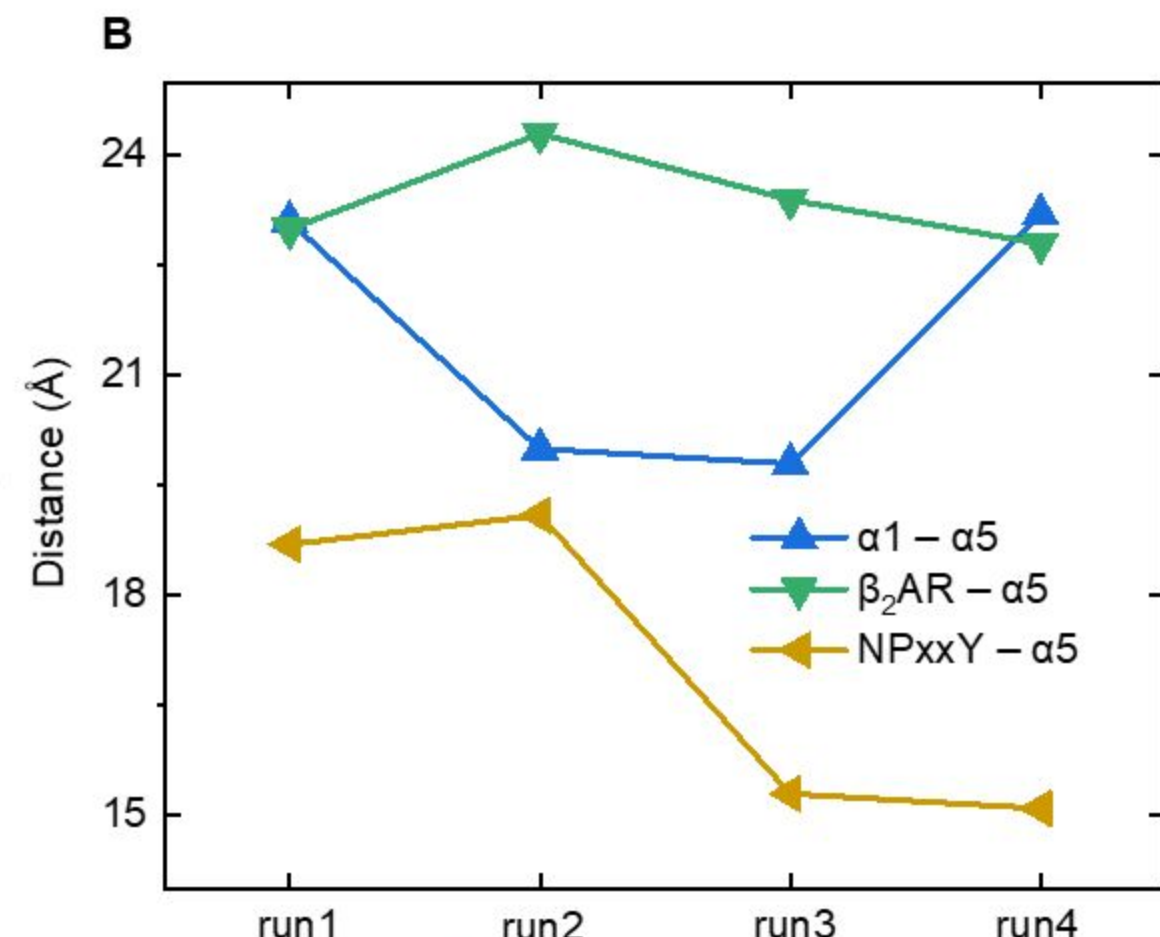
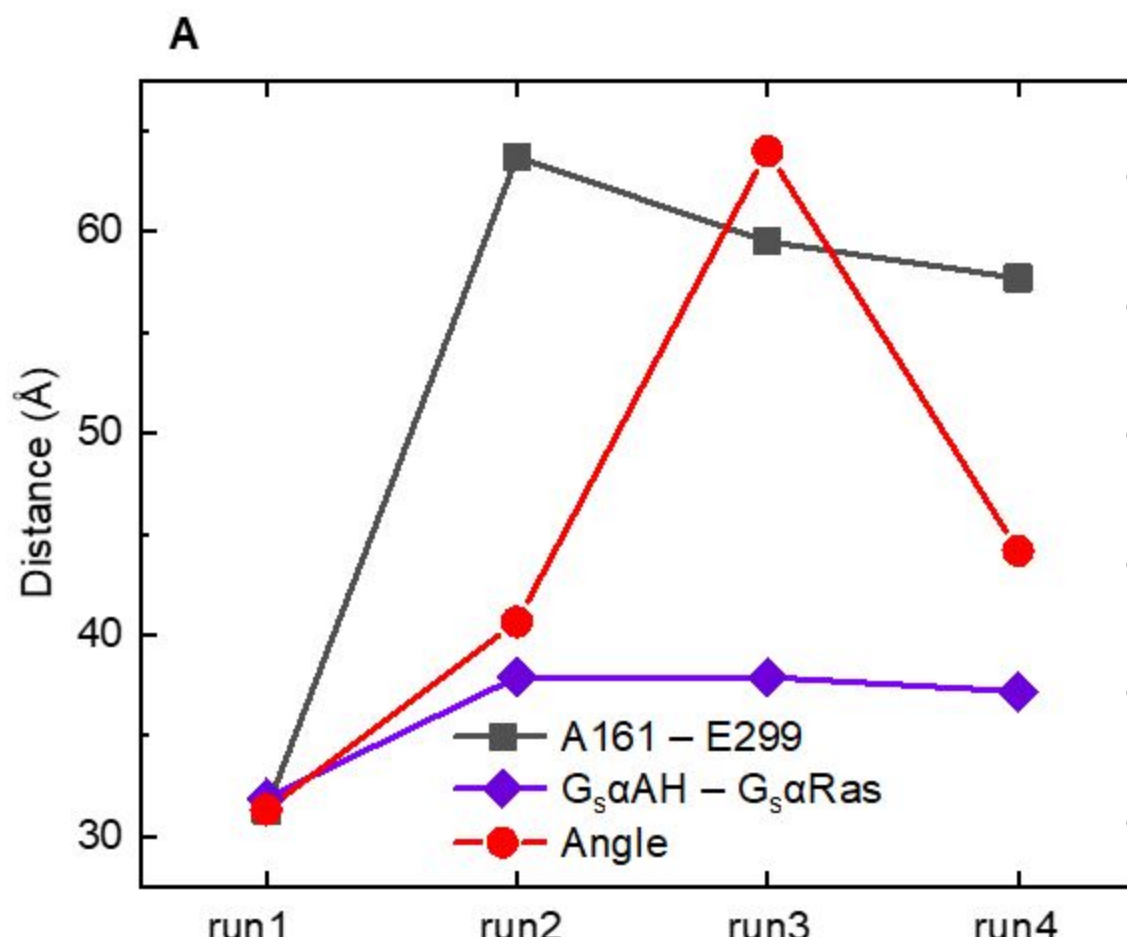
Table 2. MM-PBSA interaction free energies between β_2 AR and G_s (in kcal/mol) along with their standard errors of mean (SEM) computed using block averages, enthalpic (ΔH) and entropic ($-T\Delta S$) components (based on the last 2 μ s of Anton trajectories).

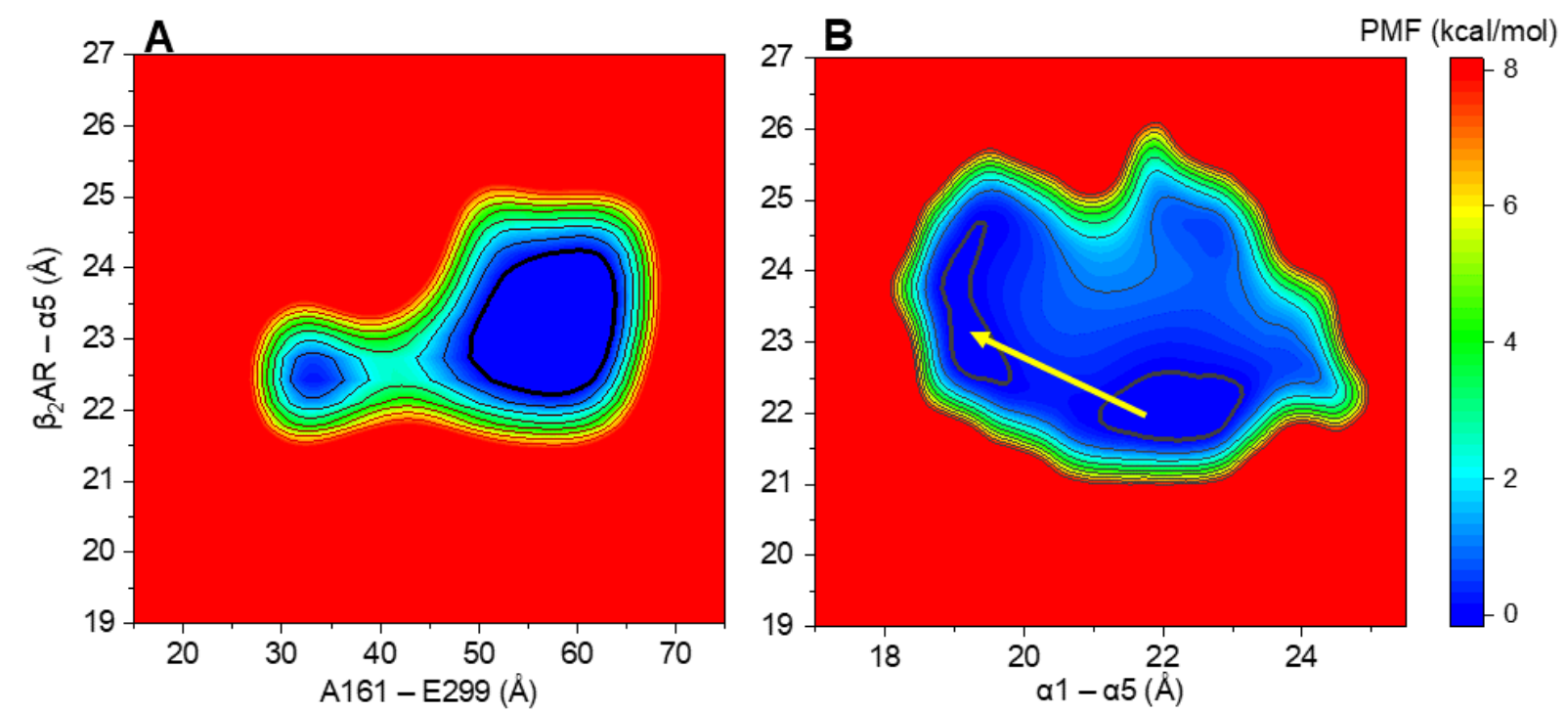
System	Time	ΔH	$-T\Delta S$	$\Delta G \pm SEM$
β_2 AR- G_s - run1	3.0 – 5.0 μ s	-145.4	105.1	-40.3 \pm 8.2
β_2 AR- G_s - run2	3.0 – 5.0 μ s	-111.8	82.9	-28.9 \pm 8.6
β_2 AR- G_s – run3	5.5 – 7.5 μ s	-154.6	105.4	-49.2 \pm 17.2
β_2 AR- G_s – run4	3.0 – 5.0 μ s	-109.6	83.6	-26.0 \pm 4.9





A**B**





Supporting Information for**Elucidation of a dynamic interplay between a beta-2 adrenergic receptor, its agonist and stimulatory G protein**

Yanxiao Han^a, John R. D. Dawson^{a,b}, Kevin R. DeMarco^a, Kyle C. Rouen^{a,b}, Slava Bekker^{a,c},
Vladimir Yarov-Yarovoy^{a,d}, Colleen E. Clancy^{a,e}, Yang K. Xiang^{e,f}, and Igor Vorobyov^{a,e,1}

^aDepartment of Physiology and Membrane Biology, University of California, Davis, CA 95616;

^bBiophysics Graduate Group, University of California, Davis, CA 95616;

^cDepartment of Science and Engineering, American River College, Sacramento, CA 95841;

^dDepartment of Anesthesiology and Pain Medicine, University of California, Davis, CA 95616;

^eDepartment of Pharmacology, University of California, Davis, CA 95616;

^fVA Northern California Health Care System, Mather, CA 95655.

¹To whom correspondence may be addressed. Email: ivorobyov@ucdavis.edu.

This PDF file includes:

Tables S1 to S5

Figures S1 to S14

Table S1. Molecular systems simulated, their simulation times (in ns or μ s), average boost potentials (ΔV) and standard deviations (std) in kcal/mol for GaMD runs. All simulation systems were first subject to 90 ns long equilibration (eq) MD runs after which microsecond-long unbiased Anton 2 MD or enhanced sampling GaMD simulations commenced. See main text “Materials and Methods” section for more details.

System name	Eq MD	Anton 2 MD		GaMD	
β_2 AR – NE(+)	90 ns	2.5 μ s		Run 1, 600 ns, $\Delta V = 14.56$, std = 4.29 Run 2, 600 ns, $\Delta V = 15.14$, std = 4.35 Run 3, 600 ns, $\Delta V = 14.65$, std = 4.29	
β_2 AR – G _s – NE(+)	90 ns	Run 1	5.0 μ s	Run 1, 600 ns, $\Delta V = 18.60$, std = 4.78	
		Run 2	5.0 μ s	Run 2, 600 ns, $\Delta V = 18.95$, std = 4.86	
		Run 3	7.5 μ s	Run 3, 600 ns, $\Delta V = 16.73$, std = 4.64	
		Run 4	5.0 μ s		

Table S2. MM-PBSA interaction free energies (ΔG) between NE(+) and β_2 AR or β_2 AR – G_s (in kcal/mol) along with their standard errors of mean (SEM) computed using block averages, enthalpic (ΔH) and entropic ($-T\Delta S$) components. Calculations were based on GaMD trajectories (600 ns each). See “Materials and Methods” section of the main text for a description of the reweighting procedure.

System	ΔH	$-T\Delta S$	$\Delta G \pm SEM$	Reweighted ΔH
β_2 AR-GaMD-run1	-26.00	8.93	-17.07 \pm 1.38	-25.96
β_2 AR-GaMD-run2	-25.61	5.30	-20.31 \pm 0.44	-26.74
β_2 AR-GaMD-run3	-26.25	7.71	-18.54 \pm 1.35	-27.69
β_2 AR-G _s -GaMD-run1	-25.87	6.58	-19.29 \pm 1.46	-27.72
β_2 AR-G _s -GaMD-run2	-24.22	7.15	-17.07 \pm 0.66	-22.21
β_2 AR-G _s -GaMD-run3	-22.22	5.19	-17.03 \pm 0.54	-21.29

Table S3. Amino acid residue (AA) contact information between different components of G_s and β₂AR proteins from Anton 2 MD runs of β₂AR – G_s – NE(+) system. Close contacts are defined as AAs within 3 Å of each other. The stable contacts are defined as AA interacting more than 50% of the simulation time. The average percentage interaction time was calculated by averaging the interaction times of the stable AA contacts in the third column.

Contacts		Number of stable contacts	Average percentage interaction time
AA in β ₂ AR interact with G _s α α5	Run 1	26	86.7%
	Run 2	22	85.0%
	Run 3	25	89.5%
	Run 4	25	88.5%
AA in G _s α α5 interact with β ₂ AR ICL3	Run 1	4	53.0%
	Run 2	3	69.8%
	Run 3	4	67.2%
	Run 4	4	62.9%
AA in β ₂ AR ICL3 interact with G _s α α5	Run 1	3	65.7%
	Run 2	3	72.5%
	Run 3	3	66.6%
	Run 4	2	75.3%
AA in β ₂ AR ICL3 interact with G _s	Run 1	5	70.6%
	Run 2	9	88.1%
	Run 3	10	78.8%
	Run 4	3	72.7%

Table S4. Pearson correlation coefficients (r) calculated for any two MD simulation averaged geometric criteria characterized in main-text Figure 4 based on Anton 2 MD runs of β_2 AR – G_s – NE(+) system: **A** – $G_{s\alpha}$ A161 to E299 distance, **B** – angle between two vectors of $G_{s\alpha}$ AH and $G_{s\alpha}$ Ras domains, **C** – $G_{s\alpha}$ AH and $G_{s\alpha}$ Ras interdomain distance, **D** – β_2 AR NpxxY to $G_{s\alpha}$ α 5 distance, **E** – β_2 AR to $G_{s\alpha}$ α 5 distance, **F** – $G_{s\alpha}$ α 1 to α 5 distance.

Row #	A and B		
1	0.61		
	A and C		
2	0.99	0.69	
	A and D	B and D	C and D
3	-0.36	-0.71	-0.46
	A and E	B and E	C and E
4	0.53	0.07	0.46
	A and F	B and F	C and F
5	-0.65	-0.63	-0.65
			D and F
			E and F
			-0.06
			-0.80

Table S5. MM-PBSA interaction free energies (ΔG) between β_2 AR and G_s (in kcal/mol), along with their standard errors of mean (SEM) computed using block averages, enthalpic (ΔH) and entropic ($-T\Delta S$) components based on GaMD trajectories (600 ns each). See the “Materials and Methods” section of the main text for a description of the reweighting procedure.

System	ΔH	$-T\Delta S$	$\Delta G \pm \text{SEM}$	Reweighted ΔH
β_2 AR- G_s -GaMD-run1	-142.3	97.9	-44.4 ± 11.9	-144.4
β_2 AR- G_s -GaMD-run2	-154.2	98.8	-55.3 ± 13.8	-135.0
β_2 AR- G_s -GaMD-run3	-119.5	94.4	-25.1 ± 18.3	-132.2

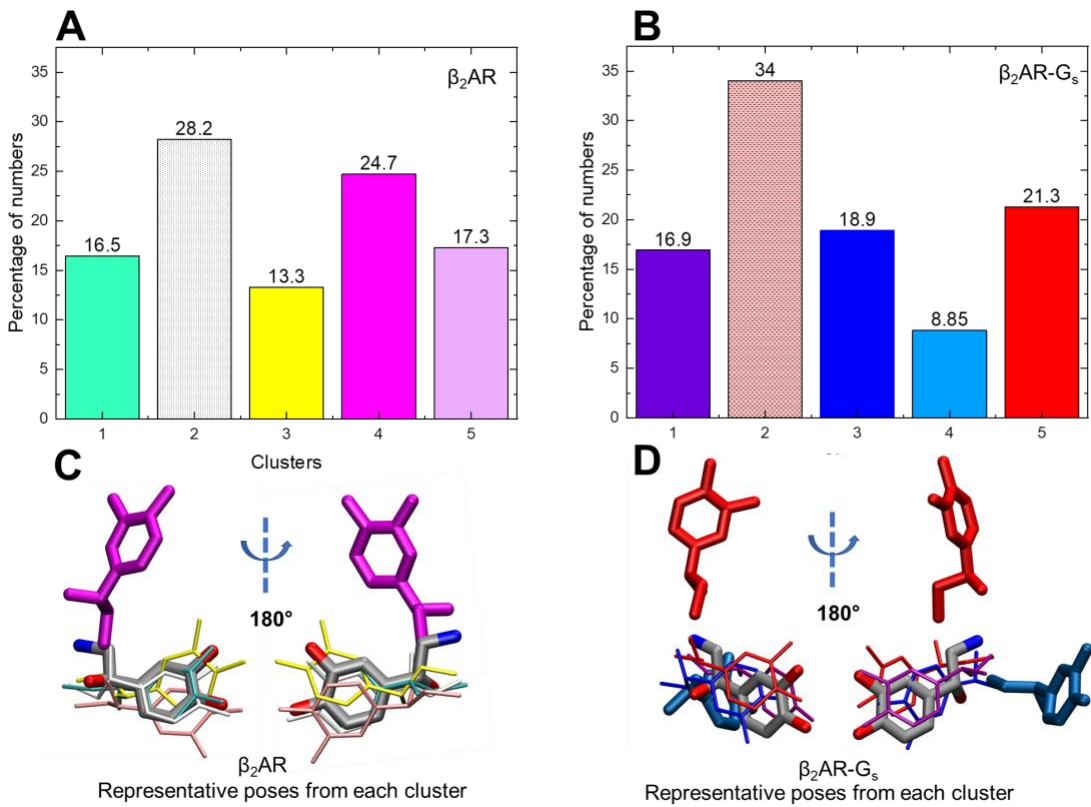


Fig. S1. **(A)** Clustering for binding poses of NE(+) in β_2 AR Anton 2 run, percentage of pose numbers out of all poses in each cluster is shown on top of each bar. **(B)** Clustering for binding poses of NE(+) in β_2 AR-G_s (Four Anton 2 runs combined), percentage of pose numbers out of all poses in each cluster is shown on top of each bar. **(C)** Representative binding poses found for β_2 AR, the coloring of molecules matches the histogram in (A), the white molecule corresponding to cluster 2 in (A). **(D)** Representative binding poses for β_2 AR-G_s, the coloring of molecules matches the histogram in (B), the red molecule with thin bonds corresponds to cluster 2.

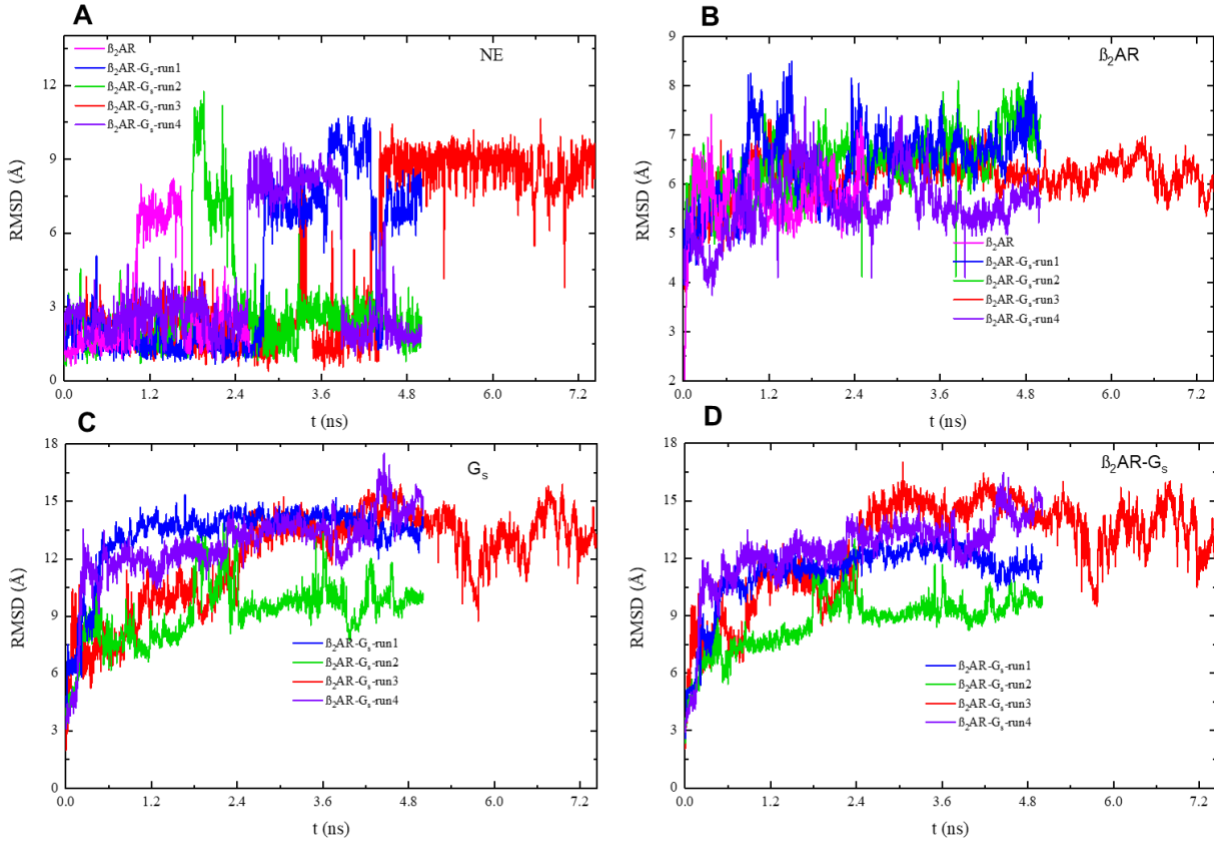


Fig. S2. RMSD time series of **(A)** NE(+) in different Anton 2 runs, trajectories were aligned to the β_2 AR without loops with the first frame as reference; **(B)** β_2 AR in different Anton 2 runs, trajectories were aligned to β_2 AR with the first frame as reference; **(C)** G_s in different Anton 2 runs, trajectories were aligned to G_s with the first frame as reference; **(D)** β_2 AR- G_s complex in different Anton 2 runs, trajectories were aligned to β_2 AR- G_s with the first frame as reference.

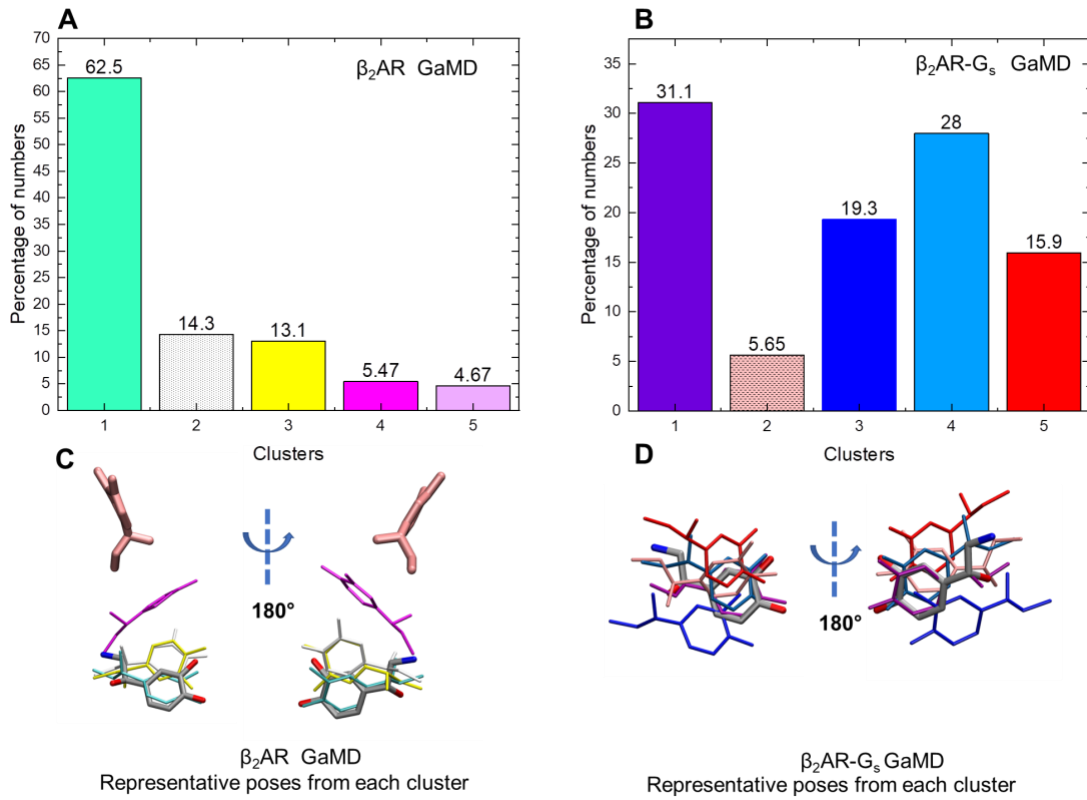


Fig. S3. **(A)** Clustering for binding poses of NE(+) in β_2 AR GaMD runs, percentage of pose numbers out of all poses in each cluster is shown on top of each bar. **(B)** Clustering for binding poses of NE(+) in β_2 AR- G_s GaMD runs, percentage of pose numbers out of all poses in each cluster is shown on top of each bar. **(C)** Representative binding poses found for β_2 AR, the coloring of molecules matches the histogram in (A), the white molecule corresponds to cluster 2 in (A). **(D)** Representative binding poses for β_2 AR- G_s , the coloring of molecules matches the histogram in (B), the pink molecule corresponds to cluster 2.

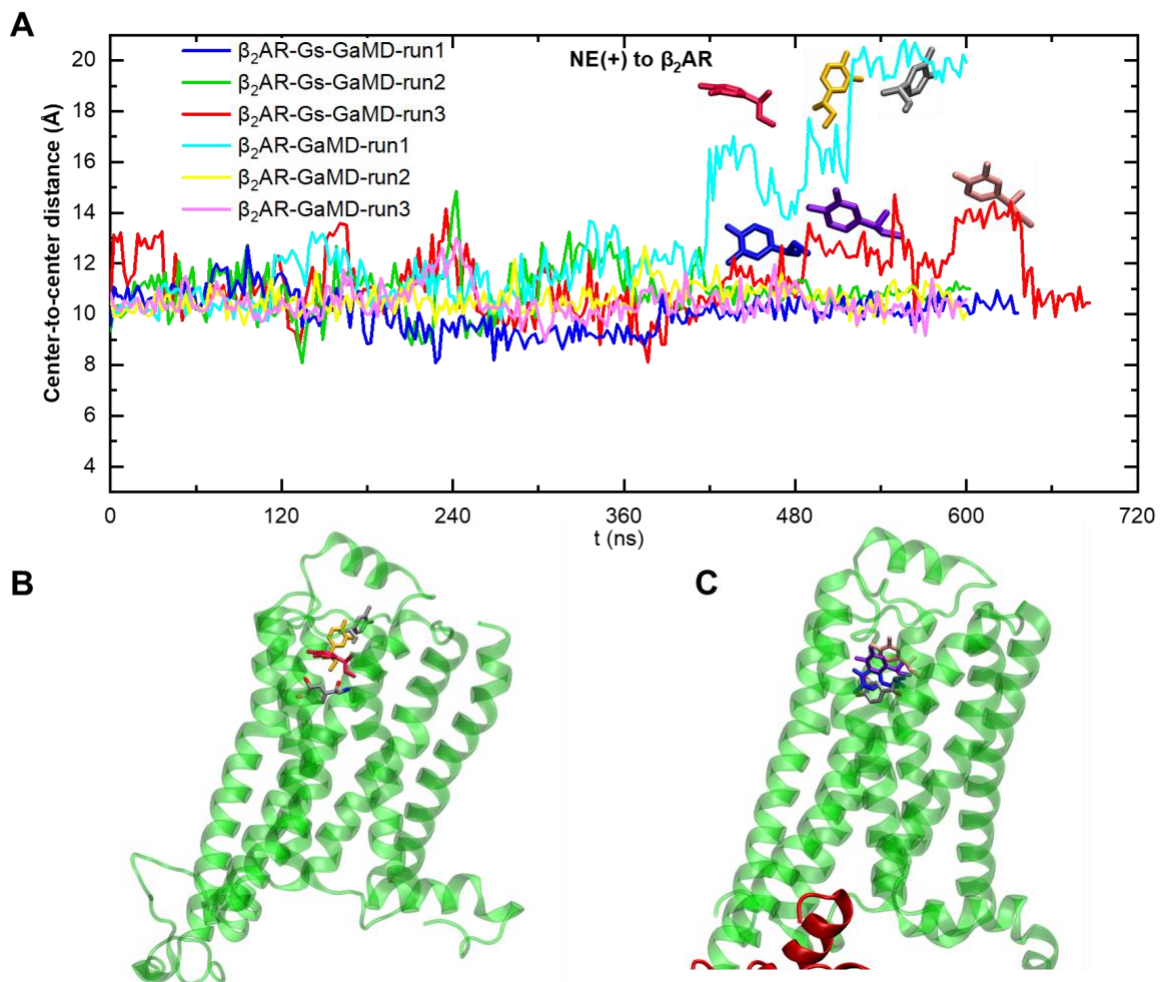


Fig. S4. **(A)** Time series of center-to-center distance between NE(+) and β_2 AR geometric centers based on GaMD simulations; **(B)** Representative binding poses of NE(+) from β_2 AR-GaMD-run1 (NE(+) colors correspond to those in panel A); **(C)** Representative binding poses of NE(+) from β_2 AR-Gs-GaMD-run3 (NE(+) colors correspond to those in panel A).

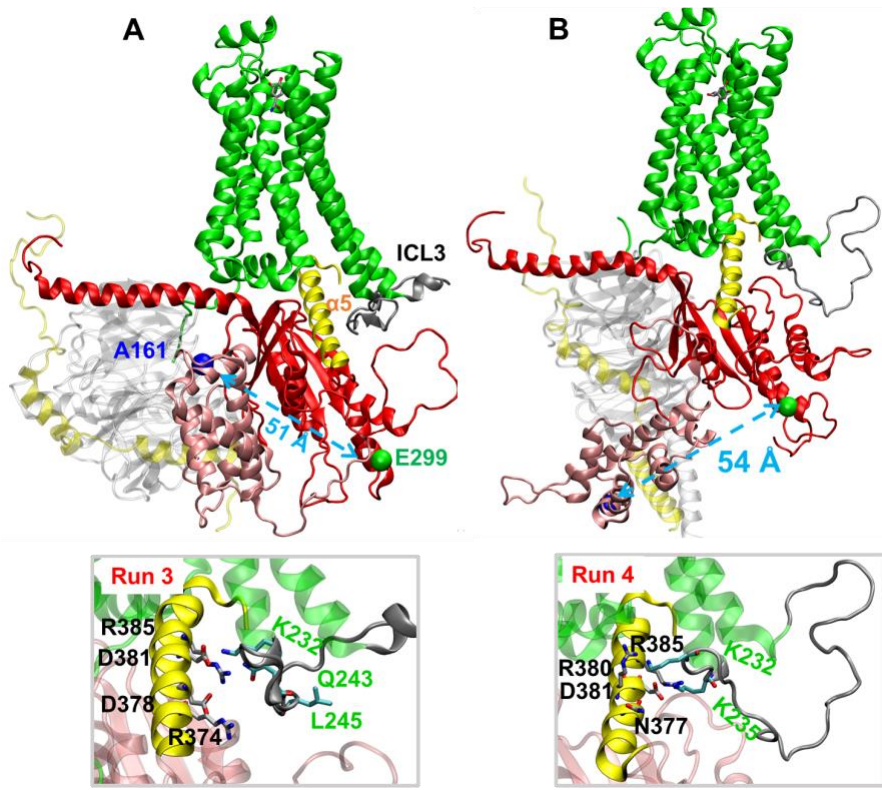


Fig. S5. All-atom Anton 2 MD simulations of the active state of the human β_2 AR- G_s complex with NE(+) bound. **(A)** run 3 with the inset at the bottom. **(B)** run 4 with the inset at the bottom. Final structures from 5 μ s long unbiased MD simulation runs on Anton 2. Individual protein chains / subunits are shown in the ribbon representation using different colors and labeled. $G_s\alpha$ α 5 helix and β_2 AR intracellular loop 3 (ICL3) are shown as yellow and dark gray. $G_s\alpha$ α -helical domain residue A161 and Ras-like domain residue E299 are shown as blue and green balls, and distances between them are shown by light-blue dashed arrows.

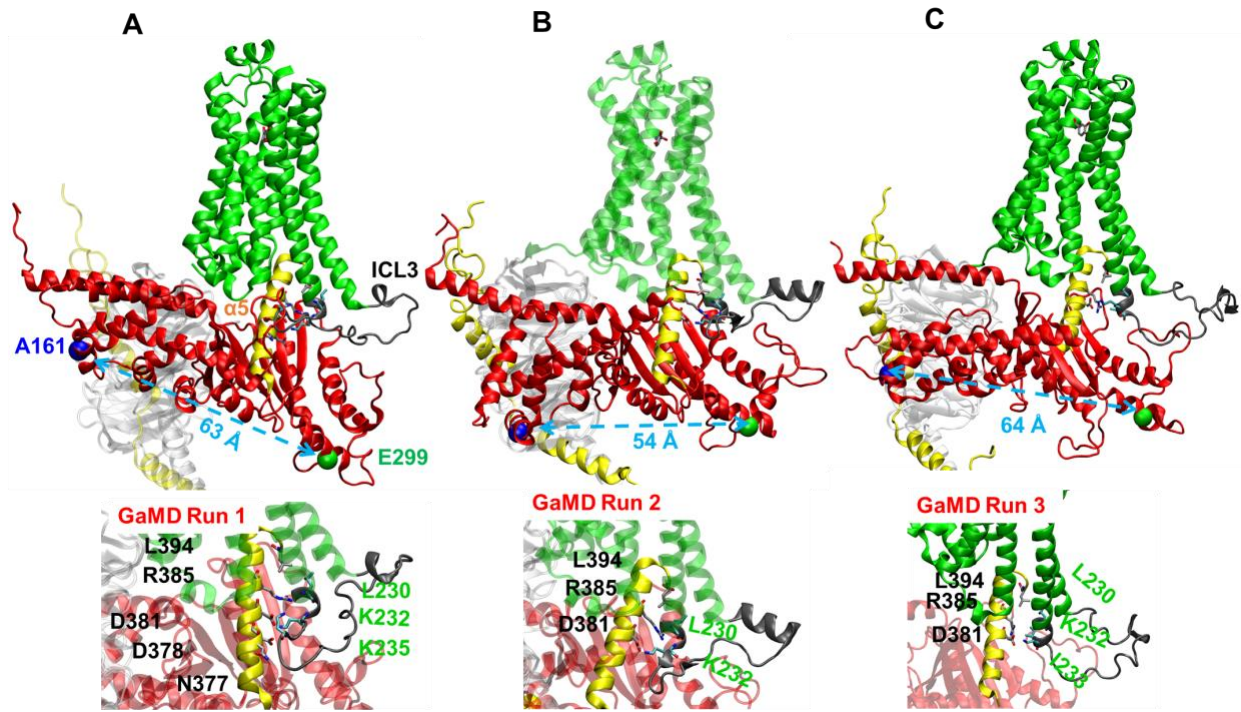


Fig. S6. All-atom GaMD simulations of the active state of the human β_2 AR-G_s complex with NE(+) bound. **(A)** GaMD run 1 with the inset at the bottom. **(B)** GaMD run 2 with the inset at the bottom. **(C)** GaMD run 3 with the inset at the bottom. Final protein structures from 600-ns long GaMD simulation runs are shown. Individual protein chains / subunits are shown in the ribbon representation using different colors and labeled. G_s α α 5 helix and β_2 AR intracellular loop 3 (ICL3) are shown as yellow and dark gray. G_s α α -helical domain residue A161 and Ras-like domain residue E299 are shown in blue and green balls, and distances between them are shown by light-blue dashed arrows.

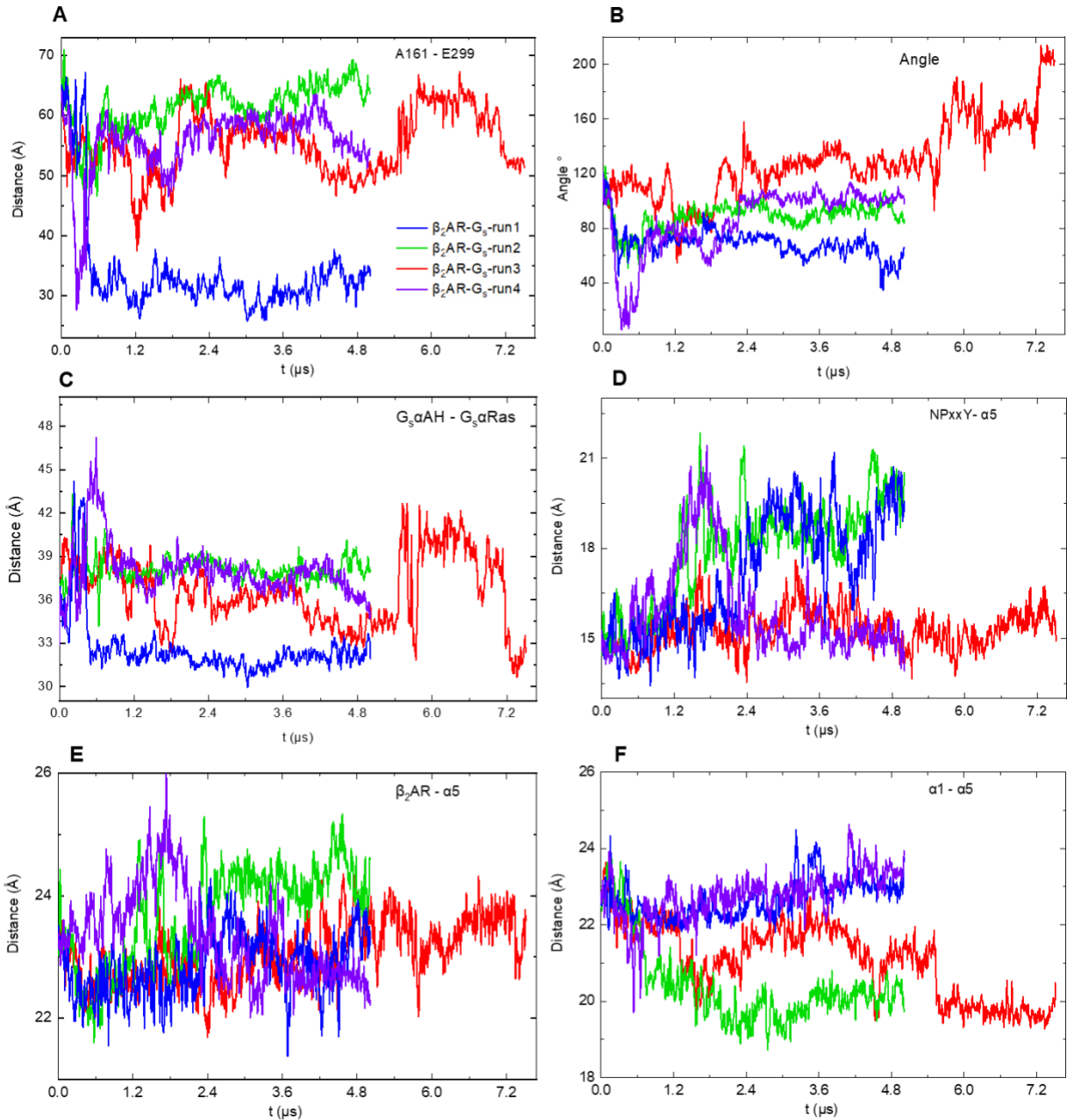


Fig. S7. Time series of geometric criteria from all-atom Anton 2 MD simulations of β_2 AR-G_s-NE(+) system: **(A)** G_s α A161 to E299 distance indicating protein conformational changes (opening or closing); **(B)** angle between two vectors found in G_s α AH and G_s α Ras domains indicating the relative orientation of two domains. Vector 1 goes through G_s α AH and A161 centers, vector 2 goes through G_s α Ras and E299 centers (see main-text Figure 4C); **(C)** distance between G_s α AH and G_s α Ras domains; **(D)** distance between NPxxY (on the TM7 of β_2 AR) and G_s α α 5 helix indicating possible partial β_2 AR-G_s dissociation; **(E)** distance between β_2 AR and G_s α α 5 indicating possible partial β_2 AR-G_s dissociation; **(F)** G_s α α 1 to α 5 distance indicating relative movement of α 1 and α 5 helices. (The geometric centers were used for the distance and angle measurements.)

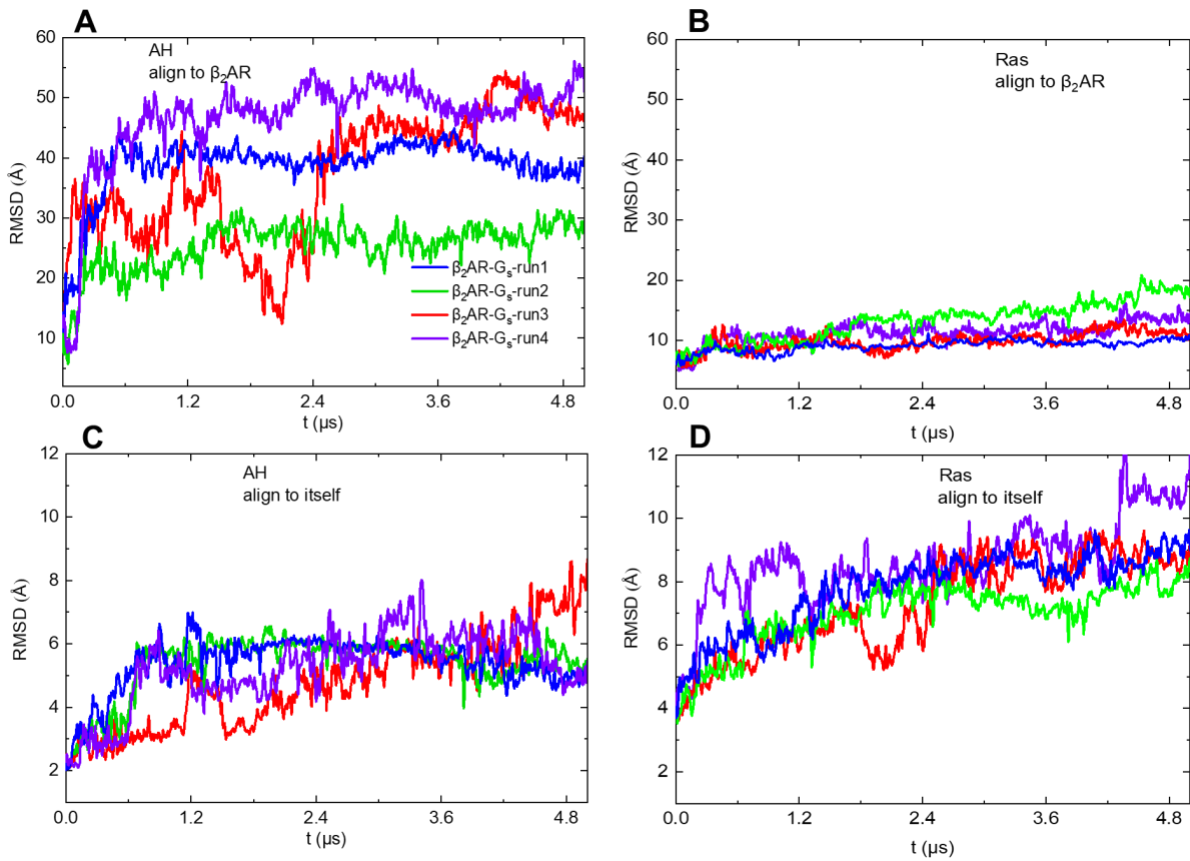


Fig. S8. RMSD time series from all-atom Anton 2 MD simulations of β_2 AR- G_s -NE(+) system: **(A)** $G_s\alpha$ AH domain C_α atoms aligned with respect to β_2 AR; **(B)** $G_s\alpha$ Ras domain C_α atoms aligned with respect to β_2 AR; **(C)** $G_s\alpha$ AH domain C_α atoms aligned with respect to its initial structure; **(D)** $G_s\alpha$ Ras domain C_α atoms aligned with respect to its initial structure.

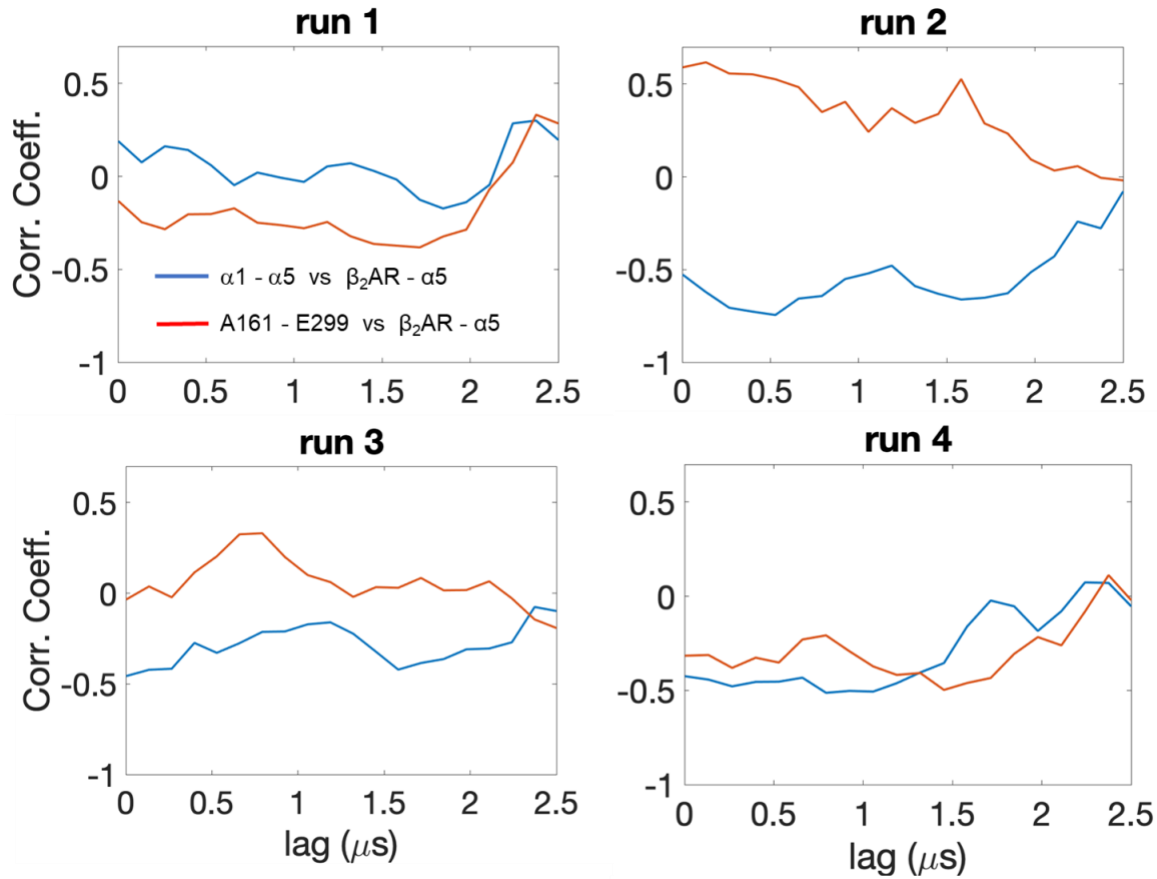


Fig. S9. Pearson correlation coefficients (Corr. Coeff) r as a function of lag time calculated for $\text{G}_s\alpha \alpha_1 - \alpha_5$ distance vs. $\beta_2\text{AR} - \text{G}_s\alpha \alpha_5$ distance (blue) and $\text{G}_s\alpha \text{A}161 - \text{E}299$ distance vs. $\beta_2\text{AR} - \text{G}_s\alpha \alpha_5$ distance (red). These data are based on all-atom Anton 2 MD simulations of $\beta_2\text{AR}-\text{G}_s\text{-NE}(+)$ system.

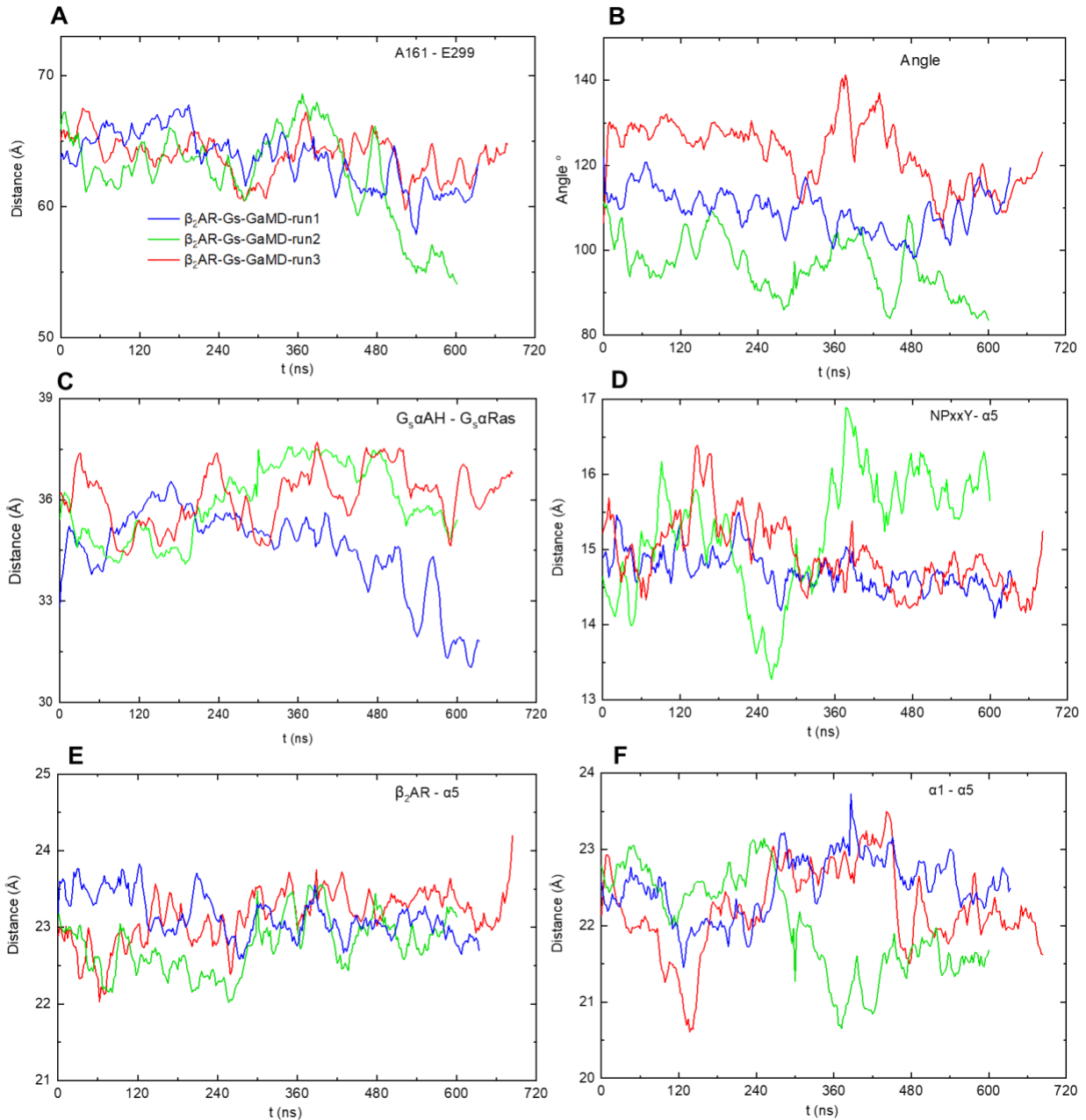


Fig. S10. Time series of geometric criteria from all-atom GaMD simulations of β_2 AR-Gs-NE(+) system: **(A)** $\text{G}_s\alpha$ A161 to E299 distance indicating protein conformational changes (opening or closing); **(B)** Angle between two vectors found in $\text{G}_s\alpha\text{AH}$ and $\text{G}_s\alpha\text{Ras}$ domains indicating the relative orientation between the two domains. Vector 1 goes through $\text{G}_s\alpha\text{AH}$ and A161 centers, vector 2 goes through $\text{G}_s\alpha\text{Ras}$ and E299 centers (see main text Fig. 4C); **(C)** Distance between $\text{G}_s\alpha\text{AH}$ and $\text{G}_s\alpha\text{Ras}$ domains; **(D)** Distance between NPxxY (on the TM7 of β_2 AR) and $\text{G}_s\alpha\alpha 5$ indicating possible partial β_2 AR-Gs dissociation; **(E)** Distance between β_2 AR and $\text{G}_s\alpha\alpha 5$ indicating possible partial β_2 AR-Gs dissociation; **(F)** Distance between $\text{G}_s\alpha\alpha 1$ and $\alpha 5$ indicating relative movement of helices $\alpha 1$ and $\alpha 5$. (The geometric centers were used for the distance and angle measurements.)

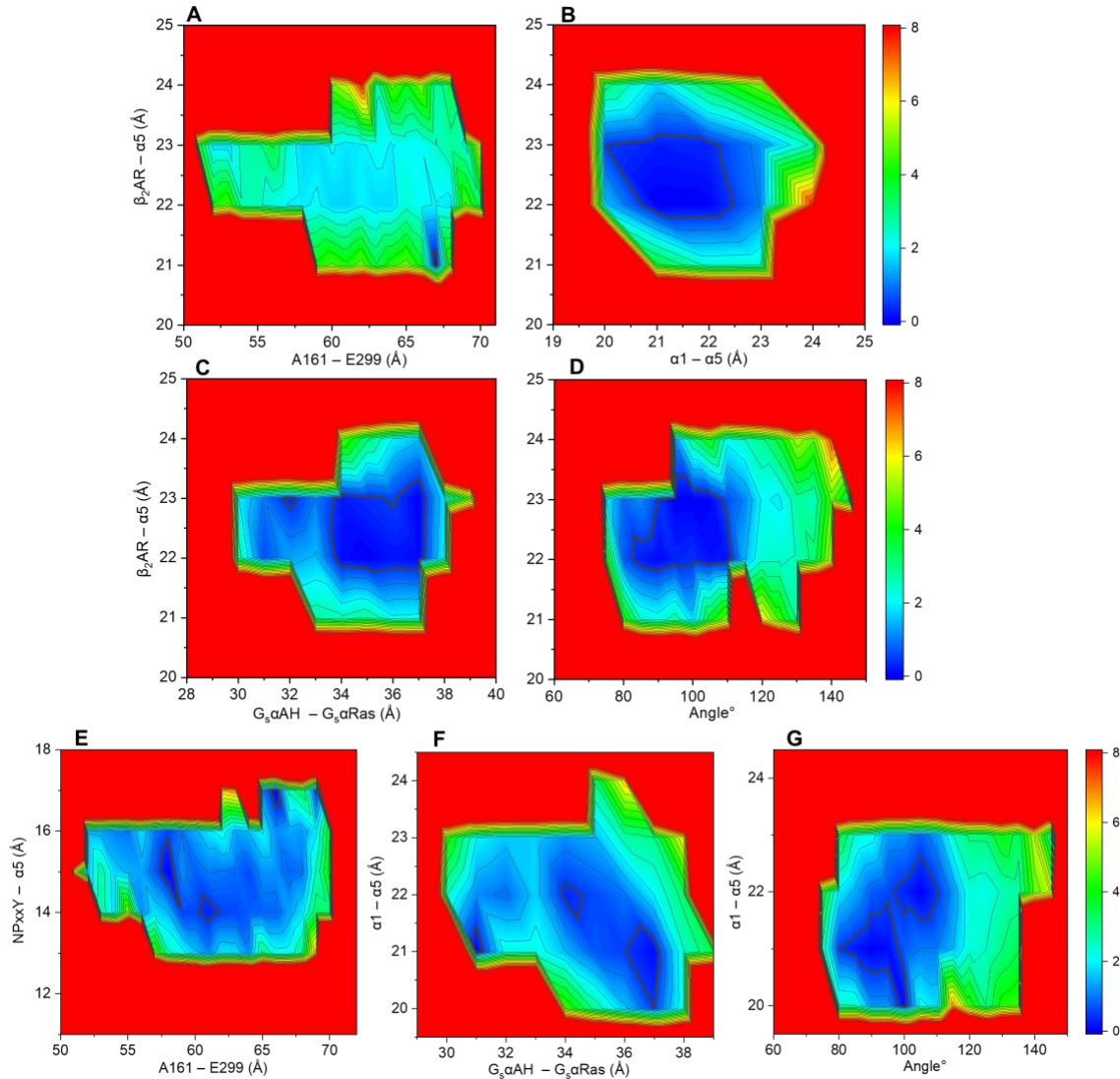


Fig. S11. 2D potential of mean force (PMF) or free energy profiles (in kcal/mol) based on $G_{s\alpha}$ conformation and its possible partial dissociation from β_2 AR from all-atom GaMD simulations of the active state of the human β_2 AR- G_s complexes with bound NE(+): **(A)** A_{161} to E_{299} distance indicating $G_{s\alpha}$ open or closed conformation is shown as X-axis. Distance between $G_{s\alpha} \alpha 5$ and β_2 AR indicating possible partial β_2 AR- G_s dissociation is shown as Y-axis. **(B)** $G_{s\alpha} \alpha 1$ to $\alpha 5$ distance is shown as X-axis. Distance between $\alpha 5$ and β_2 AR indicating possible partial β_2 AR- G_s dissociation is shown as Y-axis. **(C)** Distance between $G_{s\alpha}AH$ and $G_{s\alpha}Ras$ is set as X-axis. Distance between $G_{s\alpha} \alpha 5$ and β_2 AR indicating possible partial β_2 AR- G_s dissociation is shown as Y-axis. **(D)** Angle between two vectors, one from $G_{s\alpha}AH$ and the other from $G_{s\alpha}Ras$, is set as X-axis (shown in Figure 4C). Distance between $\alpha 5$ and β_2 AR indicating possible partial β_2 AR- G_s dissociation is shown as Y-axis. **(E)** Distance between $G_{s\alpha} A_{161}$ and E_{299} is shown as X-axis. β_2 AR $NP_{xx}Y$ to $G_{s\alpha} \alpha 5$ distance is shown as Y-axis. **(F)** Distance between $G_{s\alpha}AH$ and $G_{s\alpha}Ras$ is set as X-axis. Distance between $G_{s\alpha} \alpha 5$ and $\alpha 1$ is shown as Y-axis. **(G)** Angle between two vectors, one from $G_{s\alpha}AH$ and the other from $G_{s\alpha}Ras$ (shown in Figure 4C), is set as X-axis. Distance between $G_{s\alpha} \alpha 5$ and $\alpha 1$ is shown as Y-axis. All data are from GaMD simulations. (The geometric centers were used for the distance and angle measurements.)

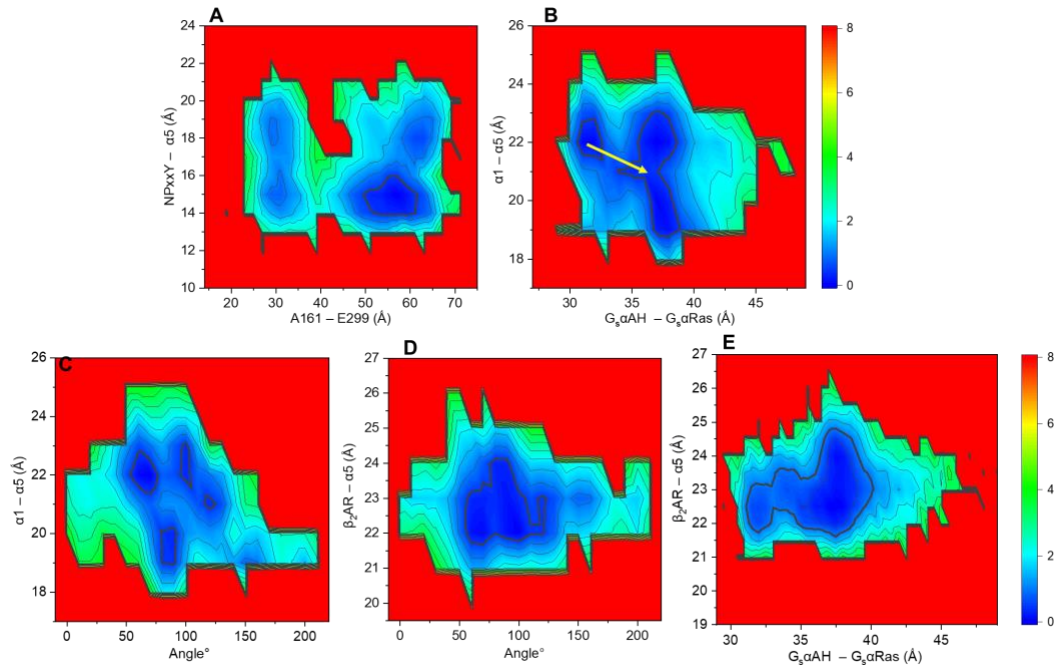


Fig. S12. 2D potential of mean force (PMF) or free energy profiles (in kcal/mol) from all-atom Anton 2 MD simulations of the active state of the human β_2 AR- G_s complexes with bound NE(+). **(A)** Distance between $G_s\alpha$ A161 and E299 is shown as X-axis. β_2 AR NPxxY to $G_s\alpha$ α 5 distance is shown as Y-axis. **(B)** Distance between $G_s\alpha$ AH and $G_s\alpha$ Ras is set as X-axis. Distance between $G_s\alpha$ α 5 and α 1 is shown as Y-axis. **(C)** Angle between two vectors, one from $G_s\alpha$ AH and the other from $G_s\alpha$ Ras, is set as X-axis. Distance between $G_s\alpha$ α 5 helix and α 1 helix is shown as Y-axis. **(D)** Angle between two vectors, one from $G_s\alpha$ AH domain and the other from $G_s\alpha$ Ras domain, is set as X-axis; distance between $G_s\alpha$ α 5 and β_2 AR is shown as Y-axis. **(E)** Distance between $G_s\alpha$ AH and $G_s\alpha$ Ras domains is set as X-axis; distance between α 5 and β_2 AR is shown as Y-axis. (The geometric centers were used for the distance and angle measurements.)

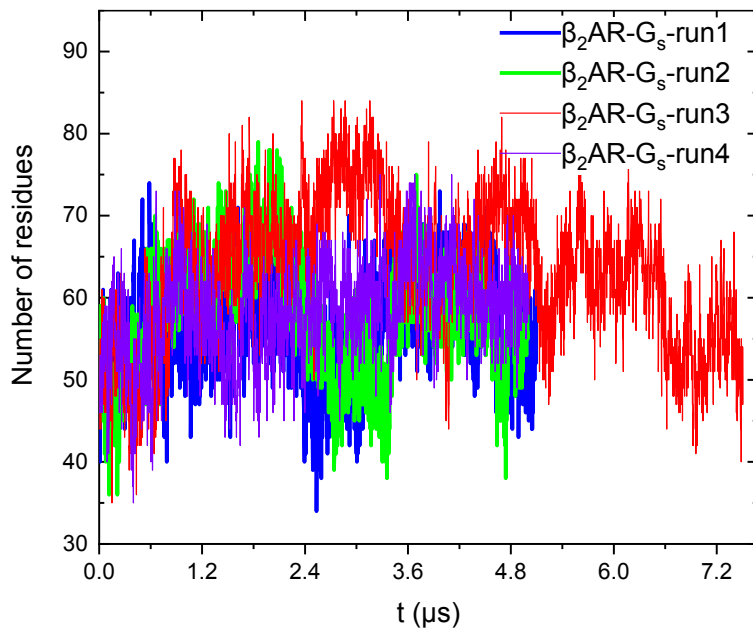


Fig. S13. Time series of the number of amino acid residues (AAs) in the binding interface between β_2 AR and G_s from all-atom Anton 2 MD simulations of β_2 AR-G_s-NE(+) system. The AAs in the binding interface were defined as those within 3 Å of either β_2 AR or G_s.

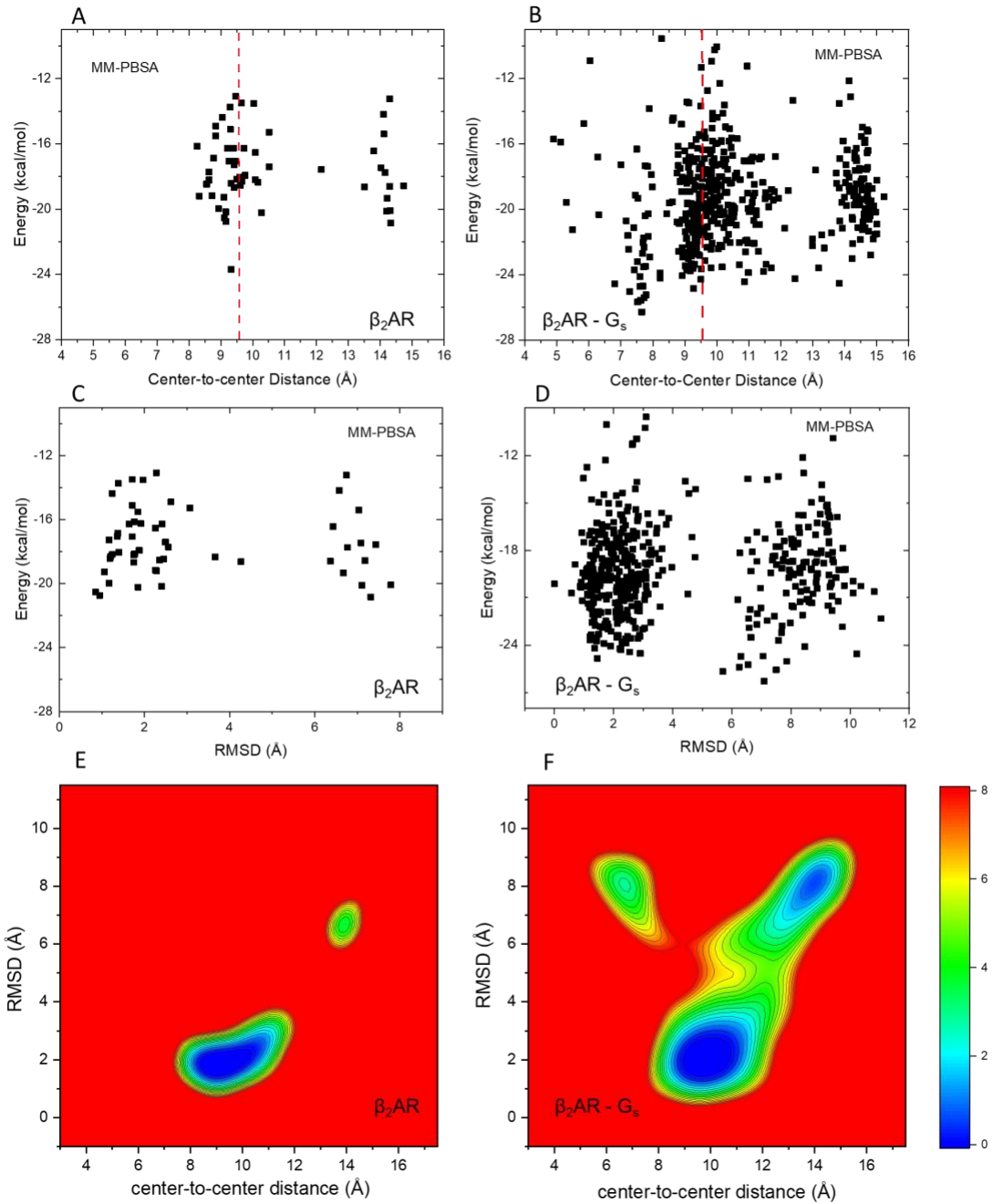


Fig. S14. **(A)** Scatter plot of MM-PBSA binding energies between NE(+) and β_2 AR with their center-to-center distances in β_2 AR only system. **(B)** Scatter plot of MM-PBSA binding energies between NE(+) and β_2 AR with their center-to-center distances in β_2 AR-G_s system. **(C)** Scatter plot of MM-PBSA binding energies between NE(+) and β_2 AR with RMSDs of NE(+) in β_2 AR only system. **(D)** Scatter plot of MM-PBSA binding energies between NE(+) and β_2 AR with RMSDs of NE(+) in β_2 AR-G_s system. **(E)** 2D PMF based on RMSD of NE(+) and center-to-center distance between NE(+) and β_2 AR captured in the β_2 AR only system. **(F)** 2D PMF based on RMSD of NE(+) and center-to-center distance between NE(+) and β_2 AR captured in the β_2 AR-G_s systems. All plots are based on Anton 2 simulations, the vertical red dashed line in panels A and B indicates the initial center-to-center distance between NE(+) and β_2 AR. (The geometric centers were used for the distance measurements.)